

**POROUS ORGANIC POLYMERS FOR
ELECTROCHEMICAL AND ENERGY STORAGE
APPLICATION**

A THESIS SUBMITTED TO

THE GRADUATE SCHOOL OF ENGINEERING AND SCIENCE OF BILKENT
UNIVERSITY

IN PARTIAL FULFILLMENT OF THE REQUIREMENTS FOR THE DEGREE OF
MASTER OF SCIENCE

IN

MATERIALS SCIENCE AND NANOTECHNOLOGY

By

Arma Musa Yau

August 2022

**POROUS ORGANIC POLYMERS FOR ELECTROCHEMICAL AND ENERGY
STORAGE APPLICATION**

By

Arma Musa Yau

August, 2022

We certify that we have read this thesis and that in our opinion it is fully adequate in scope and in quality, as a thesis for the degree of Master of Science

Dönüş Tuncel (Advisor)

Wonmi Ahn

Murat Barsbay

Approved for the graduate school of Engineering and Science:

Orhan Arıkan
Director of the Graduate School

ABSTRACT

POROUS ORGANIC POLYMERS FOR ELECTROCHEMICAL AND ENERGY STORAGE APPLICATION

Arma Musa Yau

M.S. in Materials science and nanotechnology

Advisor: Dönüş Tuncel

August 2022

The intrinsic porosity and tunable morphology of Porous Organic Polymers (POPs), materials made from organic building blocks joined by strong covalent bonds, have become appealing in the context of electrochemical applications.

In the first section of this thesis, a low-cost thiophene derivative and melamine were assembled into nitrogen and sulfur-enriched microporous organic polymer (**MOP**) using a pyrolysis-free one-pot Schiff-base type polycondensation reaction. The synthesized polymer is characterized by FT-IR, SEM, TEM, BET, XRD, XPS, TGA and UV-VIS. With $195.731 \text{ m}^2 \text{ g}^{-1}$ surface area and $0.047 \text{ cm}^3 \text{ g}^{-1}$ pore volume, the as-synthesized **MOP** has a cotton-like morphology and a micropore-dominated pore size distribution. After encapsulating it with a nickel co-catalyst, we showed that the obtained framework (**MOP**) could be used as an efficient catalyst for hydrogen evolution reaction (HER) in an alkaline electrolyte with the optimum composite (**Ni₂@MOP**) exhibiting a remarkable onset

overpotential of -66 mV. Furthermore, the optimum electrocatalyst showed good stability, delivering 90.84% faradaic efficiency (FE) after a 3.5 h chronoamperometry experiment.

In the second section, the synthesized porous organic polymer and CB[6]-porphyrin covalent organic framework were investigated for potential use as electrode materials for supercapacitors.

KEYWORDS: *Microporous Organic Polymers (MOP), Melamine, Nickel, Electrocatalytic hydrogen generation, Water splitting, Supercapacitor.*

ÖZET

ELEKTROKİMYA VE ENERJİ DEPOLAMA UYGULAMASI İÇİN

GÖZENEKLİ ORGANİK POLİMERLER

Arma Musa Yau

Malzeme Bilimi ve Nanoteknoloji, Yüksek

LisansDanışman: Dönüş Tuncel

Ağustos 2022

Güçlü kovalent bağlarla birbirine bağlı organik yapı taşlarından oluşan Gözenekli Organik Polimerlerin (POP'lar) gözenekli yapısı ve ayarlanabilir morfolojisi, bu malzemeleri elektrokimyasal uygulamalar açısından dikkat çekici hale gelmiştir.

Bu tezin ilk bölümünde, düşük maliyetli bir tiyofen türevi ve melamin, tek kap piroliz Schiff-baz tipi polikondansasyon reaksiyonu kullanılarak nitrojen ve kükürt ile zenginleştirilmiş mikro gözenekli organik polimer (MOP) haline getirilmiştir. Sentezlenen polimer FT-IR, SEM, TEM, BET, XRD, XPS, TGA ve UV-VIS ile karakterize edilmiştir.

195.731 m² g⁻¹ yüzey alanı ve 0.047 cm³ g⁻¹ gözenek hacmi ile sentezlenen MOP, pamuk benzeri bir morfolojiye ve mikro gözenekli yapının baskın olduğu bir gözenek boyutu dağılımına sahiptir. Bir nikel yardımcı katalizör ile sarmalandıktan sonra, elde edilen yapının (MOP), -66 mV gibi belirgin bir başlangıç yüksek potansiyel değerine sahip olan optimum bir kompozit (Ni₂@MOP) ile alkali elektrolitte hidrojen gelişim reaksiyonu (HER) için verimli bir katalizör olarak kullanılabileceğini gösterdik. Ayrıca, optimum

elektro-katalizör, 3.5 saatlik bir kronoamperometri deneyinden sonra 90.84 % faradik verim (FE) sağlayacak şekilde iyi bir stabilite özelliği gösterdi.

İkinci bölümde, sentezlenen gözenekli organik polimer ve CB[6]-porfirin kovalent organik yapının süperkapasitörlerde elektrot malzemeleri olarak potansiyel kullanımı araştırılmıştır.

ANAHTAR KELİMELER: *Mikro Gözenekli Organik Polimerler (MOP), Melamin, Nikel, Elektrokatalitik hidrojen üretimi, Su parçalama, Süperkapasitör*

Acknowledgment

I would like to extend to my sincere gratitude to my supervisor, professor Dönüş Tuncel for believing in me and providing me with the necessary support and guidance during my research that has greatly helped me complete my master. Being part of Tuncel's research group has been rare a rare privilege and honor.

Secondly, I am thankful to my committee members, Asst. Prof. Wonmi Ahn and Prof. Murat Barsbay, for taking their valuable time to review my thesis.

Many thanks also to my colleagues in Tuncel's research group, especially Aysan Khaligh, whose valuable support has contributed significantly to the success of my program.

Finally, I would like to sincerely appreciate and deeply thank my family members, especially daughter, Mariyya, and my lovely wife, Fatima. Your unwavering support and daily dose of love gave me the energy to keep going and never give up. Thank you, and God bless!

Contents

CHAPTER 1	1
INTRODUCTION	1
1.1 Classification of Hydrogen	2
1.2 Electrochemical Water Splitting	3
1.3 Hydrogen Evolution Reaction (HER)- The Mechanism	5
1.4 Evaluation Approaches for Her Electrocatalysts	7
1.4.1 Overpotential	7
1.4.2 Tafel Plot	8
1.4.3 Stability.....	8
1.4.4 Electrochemical Impedance Spectroscopy (EIS)	9
1.4.5 Faradaic Efficiency (FE)	9
1.4.6 Turnover Frequency (TOF)	10
1.5 Electrocatalysts For Hydrogen Evolution Reaction	10
1.6 Porous Organic Polymers (POPs) for HER	12
1.6.1 Heteroatom-containing POPs	12
1.6.2 Metal Encapsulated POPs.....	14
1.7 Porous Organic Polymers for Supercapacitors	15
1.8 Aim of The Study	18
CHAPTER 2	20
EXPERIMENTAL AND INSTRUMENTATION	20
2.1 Chemicals	20

2.2 Synthesis	20
2.3 Structural Setermination and Characterization Techniques	21
2.3.1 Scanning Electron Microscope.....	21
2.3.2 X-ray Photoelectron Spectroscopy	22
2.3.3 X-ray Diffraction	22
2.3.4 Infrared Spectroscopy.....	23
2.3.5 UV-VIS Spectroscopy	23
2.3.6 Transmission Electron Microscopy	23
2.3.7 Thermogravimetric Analysis	24
2.3.8 Nitrogen Adsorption Measurement	24
2.4 Preparation of Working Electrodes	25
2.4.1 Hydrogen Evolution Reaction	25
2.5.2 Supercapacitors.....	25
2.5 Electrochemical Measurement	25
CHAPTER 3	27
RESULTS AND DISCUSSION	27
3.1 Section 1: Microporous Organic Polymer (MOP) for Hydrogen Evolution Reaction	27
3.2 Synthesis and Characterization of MOP	27
3.3 Evaluation of Electrocatalytic HER activity of MOP	36
3.4 Pre- and Post-Catalytic Characterization of Ni₂@MOP	45
3.5 Section 2: Porous Organic Polymers as Electrode Materials for Supercapacitors	52

3.5.1 Evaluation as Electrode Materials for Supercapacitors.....	54
CHAPTER 4	57
CONCLUSION AND FUTURE WORKS	57
REFERENCES	59
APPENDIX	69

LIST OF FIGURES

Figure 1-1. Illustration of electrocatalytic hydrogen production in 3-electrode cell comprising of working electrode (WE), reference electrode (RE), and counter electrode (CE).....	5
Figure 1-2: Illustration of synthesis of DBT-MA-COF and its electrochemical performance. Reprinted from ref [40] Copyright (2021), with permission from Elsevier.	17
Figure 3-1: FT–IR spectra of MOP compared to its monomers, melamine (Me), and 2,5-thiophenedicarboxaldehyde (Th).	30
Figure 3-2: UV spectrum of MOP, its monomers, and the mechanical mixture of the monomers.....	30
Figure 3-3. High resolution XPS spectra of (a) C 1s, (b) N 1s (c), and S 2p for MOP ...	31
Figure 3-4: (a) TEM; (b) SEM Images ;(c) Elemental Mappings; (d) SEM/EDX spectrum of MOP and the corresponding atomic percentage of elements; of Pristine MOP.....	32
Figure 3-5: (a) XRD spectrum of MOP; (b) XRD spectrum its monomers.....	33
Figure 3-6: N ₂ physisorption isotherm of MOP.....	34
Figure 3-7: BJH pore size distribution of MOP.....	34
Figure 3-8: Multipoint BET of MOP (R ² = 0.9999).	35
Figure 3-9: TGA graph of MOP, its monomers and mechanical mixture of the monomers	36
Figure 3-10 (a)LSV polarization curves for pristinne MOP at 10 mVs ⁻¹ in different electrolytes (b) LSV polarization curves of Ni@MOP catalysts with varying Ni content in comparison with bare FTO and standard 10% Pt/C , measured at 10 mVs ⁻¹ in 0.5 M KOH, (c) The corresponding Tafel plots in the linear region, and (d) The iR-corrected LSV curve of the optimum Ni₂@MOP catalyst compared to the standard 10% Pt/C measured at 10 mVs ⁻¹ in 0.5 M KOH.	40

Figure 3-11: (a) Polarization curves of Ni ₂ @MOP with and without manually IR correction (b) Polarization curves of 10 % Pt with and without manually IR correction.	41
Figure 3-12: (a) The Nyquist plots of various Ni@MOP catalysts recorded at -0.64 V vs RHE in 0.5 M KOH (b) The capacitive currents (Δj) at 1.02 V vs RHE as a function of scan rate for Ni ₂ @MOP catalyst in 0.5 M KOH ($\Delta j = j_{anodic} - j_{cathodic}$), (c) chronoamperometry of Ni ₂ @MOP under constant potential of -0.64 V vs RHE in 0.5 M KOH, and (d) the corresponding polarization curves of Ni ₂ @MOP before and after 3.5 h stability experiment obtained at 10 mVs ⁻¹ in 0.5 M KOH. (e) CV of Ni ₂ @MOP at different scan rates	45
Figure 3-13: (a) FTIR spectrum of pristine MOP and Ni ₂ @MOP; High resolution XPS (b) N1s (d) Ni 2p (d) S 2p for Ni ₂ @MOP	47
Figure 3-14: Proposed Ni mechanism of interaction with MOP	48
Figure 3-15: TEM images of Ni ₂ @MOP	48
Figure 3-16: SEM images of Ni ₂ @MOP (a) before and (c) after 3.5 h chronoamperometry experiment at -0.64 V vs. RHE in 0.1M KOH, (b, d) corresponding elemental mapping images of elements C, N, O, S, and Ni.....	51
Figure 3-17: XPS data of Ni ₂ @MOP (a) before and (b) after 3 h chronoamperometry experiment at -0.64 V vs. RHE in 0.5M KOH.....	52
Figure 3-18: Cyclic Voltammetry (CV) curves of (a) MOP; (b) CB[6]-porphyrin framework; at a scan rate of 100mVs ⁻¹ in 6M KOH.....	56
Figure 3-19: Galvanostatic Charge-Discharge (GCD) curves of (a) MOP at current density of 0.1mA g ⁻¹ ; (b) CB[6]-porphyrin framework at a current density of 0.001mA ⁻¹	56

LIST OF TABLES

Table 3-1: Electrochemical parameters of the various electrocatalysts investigated towards HER in 0.5 M KOH.....	42
Table 3-2: Resistance values obtained from Nyquist plots for samples with various Ni loading.....	45
Table A.1. A comparison of electrochemical parameters of different non-noble metal electrocatalysts.....	69

ABBREVIATIONS

BET, Brunauer–Emmett–Teller

BJH, Barrett–Joyner–Halenda

CA, Chronoamperometry

CB, Cucurbituril

EDX, Energy Dispersive X-ray

EIS, Electrochemical Impedance Spectroscopy

FE, Faradaic Efficiency

FT-IR, Fourier-transform infrared spectroscopy

HER, Hydrogen Evolution Reaction

LSV, Linear Sweep Voltammetry

Me, Melamine

MOP, Microporous Organic Polymer

Ni, Nickel

POP, Polymer Organic Polymer

SEM, Scanning Electron Microscopy

TEM, Transmission Electron Microscopy

Th, 2,5-thiophenedicarboxaldehyde

TOF, Turnover Frequency

UV-vis, Ultraviolet–visible

XRD, X-ray Diffraction

XPS, X-ray Photoelectron Spectroscopy

η , Overpotential

$\eta @ 10 \text{ mA cm}^{-2}$, Overpotential at 10 mA cm^{-2}

CHAPTER 1

INTRODUCTION

Due to global development and population growth, global energy demand has continued to rise quickly during the last century.[1] The demand for energy is predicted to rise from 16 Terawatts (TW) in 2010 to 23 TW in 2030, and perhaps even 30 TW in 2050. According to recent statistics, 79.5 % percent of this total energy consumed comes from conventional sources such as oil, coal, and natural gas, while renewable sources like hydropower, wind, biopower, and solar photovoltaics provide only 20.5% of global energy consumed.[2] The impending exhaustion of the non-renewable energy sources, as well as the ensuing energy and climate catastrophe, require the urgent development of alternative, clean, and renewable energy sources for long-term sustainability. Many alternative fuels, such as biodiesel, LPG, hydrogen, boron, and solar fuels, have been attempted. Compared to the other fuels, hydrogen has a lot of promise for use as an alternative fuel because it is the most abundant naturally occurring element. Furthermore, H₂ has the highest gravimetric energy density and produces solely pollution-free water as a combustion byproduct, it is a suitable energy transporter and a viable option for future low-carbon energy systems.[3] However, most H₂ is now created by steam reforming fossil fuels. This method of production not only utilizes low-conversion-rate fossil fuels but also releases CO₂. To this purpose, a clean, renewable, and efficient way of producing hydrogen without causing additional difficulties is critical to the hydrogen economy's effective implementation.[4]

1.1 Classification of Hydrogen

Hydrogen is differentiated using color-band nomenclature and can be classified into Gray, Blue, and Green hydrogens, based on manufacturing methods[5].

Gray hydrogen is the least renewable kind of hydrogen because it is obtained from natural gas and produced using fossil fuels. Gray hydrogen accounts for the majority of hydrogen produced today. It is pretty affordable and is widely utilized in the chemical sector for fertilizer production and oil refining. It is made via reforming natural gas, which is a method of rearranging hydrocarbon molecules' molecular structure. Through a catalytic chemical reaction, methane—the primary component of natural gas—is combined with steam at a high temperature, releasing almost 10 kg of CO₂ for every 1 kg of hydrogen produced.[6],[7]

Similarly, blue hydrogen is produced in the same processing technique with gray hydrogen. However, the control of CO₂ is a significant distinction. The CO₂ created by blue hydrogen does not escape into the atmosphere. Instead, it is caught and stored separately at the manufacturing facility using a technology known as Carbon Capture and Storage (CCS) Technology[8]. Storage, on the other hand, is both expensive and logistically challenging, thus, presently making it economically infeasible for commercial adoption.[9],[10]

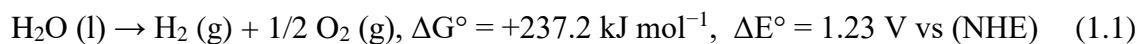
Brown hydrogen is produced through the coal gasification method. Here, coal is transformed from a solid to a gas in the process of coal gasification. In gasification systems, the coal is partially oxidized with steam and oxygen in a high-temperature, high-pressure

process. As a result, synthesis gas is produced, which is a mixture of carbon monoxide (CO), hydrogen, carbon dioxide, and some steam. The synthesis gas, also known as syngas, is then combined with water to boost hydrogen production. Brown hydrogen is the least environmentally friendly, producing 12 tons of CO₂ for every tone of hydrogen produced.[11]

Green hydrogen is a step closer to true sustainability.[12] This type of hydrogen is produced completely differently from gray or blue hydrogen. The method uses electrolysis, which involves applying electrical energy to water to separate hydrogen and oxygen molecules. This method produces a complete loop of sustainable energy with no hazardous gases produced at any step in the manufacturing process, making it the ultimate goal in the hydrogen fuel sector. Although green hydrogen appears to be the best option, it is challenging to produce due to the high cost of electrolysis equipment. [13],[14]

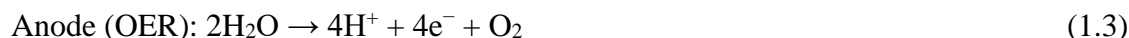
1.2 Electrochemical Water Splitting

Water is both the only starting molecule and a byproduct in the cycle of the hydrogen economy, making electrochemical water splitting to make hydrogen (and oxygen) a clean, effective, and sustainable alternative to fossil fuel. The two halves of the water-splitting reaction are the hydrogen evolution reaction (HER) at the cathode and the oxygen evolution reaction (OER) at the anode. The dissociation of water with the normal hydrogen electrode (NHE) requires a thermodynamic potential of 1.23 V and a Gibbs free energy (G) of 273 kJ mol⁻¹, as shown below.[15]

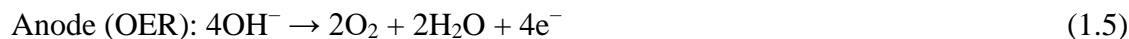


Higher potential (otherwise known as overpotential) is needed to drive hydrogen evolution (HER), and oxygen evolution (OER) processes at a quantifiable current density due to their poor kinetics. The potential difference between the necessary and determined thermodynamic parameters of a specific electrochemical reaction is known as overpotential. Electrocatalysts' job is to minimize this overpotential as much as feasible. Based on the electrolyte being used, the electrochemical water splitting goes through various mechanisms:

Under acidic medium,



Under basic medium,



In acidic environments, water splits into oxygen gas and protons, which are subsequently reduced at the cathode to generate hydrogen gas. In contrast, a lack of proton forces charge transfer by hydroxide ions in a basic medium. Changes in potential are thought to occur at the working electrode in water electrolysis. The working electrode's potential is measured relative to a known potential of a non-polarizable electrode (reference electrode) whose

equilibrium potential remains constant throughout the experiment. As a result, instead of using the Normal Hydrogen Electrode (NHE), the data are reported as a function of the Reversible Hydrogen Electrode (RHE), which takes pH fluctuations into account, as shown below:

$$E_{\text{RHE}} = E_{\text{NHE}} + 0.0059 \times \text{pH} \quad (1.6)$$

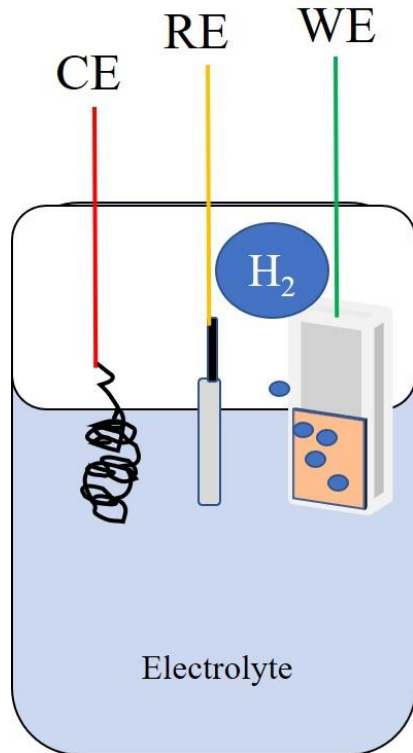
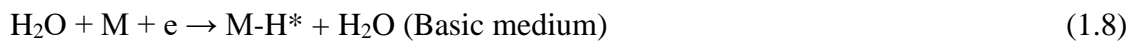


Figure 1-1. Illustration of electrocatalytic hydrogen production in 3-electrode cell comprising of working electrode (WE), reference electrode (RE), and counter electrode (CE)

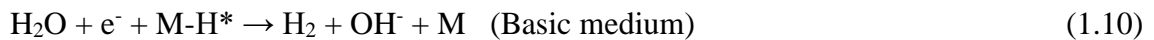
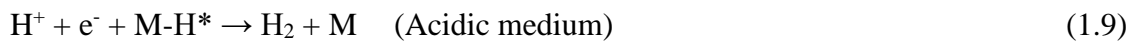
1.3 Hydrogen Evolution Reaction (HER)- The Mechanism

In the electrochemical HER process for reducing protons in acidic media or water molecules in alkaline media to hydrogen molecules (H_2) on the surface of an electrode with a minimum, the external voltage applied, three probable primary phases are involved.[16] The Volmer reaction (equations 1.7 and 1.8) is the initial step, in which a proton combines with an electron to produce an adsorbed hydrogen atom (H^*) on the electrode material surface (M). In acidic and alkaline electrolytes, the hydronium cation (H_3O^+) and water molecule are the proton suppliers. Another proton diffuses to the H^* during the Heyrovsky step, which subsequently interacts with a second electron to form H_2 . In the Tafel step, two nearby H^* mix on the electrode's surface to evolve H_2 . The Heyrovsky reaction (equations 1.9 and 1.10) or the Tafel reaction (equation 1.11), or both, may result in the production of H_2 . The overall mechanism can be written as:[16]

Electrochemical hydrogen adsorption (Volmer step)



Electrochemical desorption (Heyrovsky step)



Chemical desorption (Tafel step)



1.4 Evaluation Approaches for HER Electrocatalysts

1.4.1 Overpotential

The Nernst equation states that the HER's Nernst potential with respect to the normal hydrogen electrode (NHE) is zero under normal conditions. However, to overcome kinetic obstacles caused by difficulties such as high activation energy and low energy efficiency, practical HER processes require a higher applied voltage (also known as overpotential). The catalyst's corresponding overpotential (η) is the difference between equilibrium potential (E_{HER}) and the required potential to drive HER. Thus, the applied potential (E or $E_{\text{uncorrected}}$) can be expressed as

$$E = E_{\text{HER}} + \eta \quad (1.12)$$

Meanwhile, internal resistance (R_s) resulting from the internal resistance of the electrocatalyst, the solvent resistance, and the distance between the working and the reference electrodes introduces ohmic potential drop, which necessitates correction/compensation in potential current density curve. Hence, the potential required to drive HER is further expressed as.

$$E = E_{\text{HER}} + \eta + iR \quad (1.13)$$

where iR represents the ohmic potential drop of a current flow in the measurement system

Overpotential η_{10} at 10mAcm^{-2} usually serves as the basis for comparing the activities of various electrocatalysts because the current density of 10mAcm^{-2} is equivalent to the 12.3% efficiency of a solar water-splitting device. A smaller η_{10} suggests a higher activity of the catalyst.[17]

1.4.2 Tafel Plot

A plot of overpotential(η) vs log current density is known as a Tafel plot, which is a useful tool for evaluating kinetic parameters. The Tafel slope (b) is a catalyst's intrinsic feature that is directly related to the HER rate. It is usually obtained from the Tafel equation ($\eta = b \log(j/j_0)$, where j and j_0 are the current density and exchange current density, respectively). By plotting η against $\log |j|$, the Tafel slope (b) can be obtained from the linear part of the Tafel plot. The j_0 is a key kinetic parameter that describes an electrocatalyst's inherent catalytic activity under reversible conditions, and it may be calculated by assuming its η is zero. The smaller 'b' indicates that less current density increase is necessary, indicating quicker electron-transfer kinetics. A high j_0 and a modest 'b' are required for a high-performance electrocatalyst.[18]

1.4.3 Stability

Another essential criterion to consider while evaluating an HER catalyst's possible practical uses is its stability. Cyclic voltammetry (CV) and galvanostatic or potentiostatic electrochemical methods are used for durability tests. By conducting CV in the region, including the onset potential, the voltammetric approach compares the changes in

overpotential before and after a specific cycle run (e.g., 10,000 runs). After numerous potential cycles, an insignificant shift in the overpotential indicates that the electrocatalyst is stable. The galvanostatic (or potentiostatic) strategy involves monitoring the electrocatalyst's potential (or current density) fluctuation over time while keeping a steady current density (or overpotential). The longer time without a potential (or current) change indicates that the system is stable.[19]

1.4.4 Electrochemical Impedance Spectroscopy (EIS)

As previously stated, the HER often follows the Volmer (1.7 and 1.8), Heyrovsky (1.9 and 1.10), or Tafel (1.11) stages. The rates/kinetics of the overpotentially adsorbed hydrogen are assessed using EIS, assuming a Langmuir adsorption isotherm. EIS Nyquist plots also provide the uncompensated ionic and ohmic resistance of the electrochemical measuring equipment and the R_{ct} of a catalyst. R_{ct} refers to the charge transfer process at an electrode's interface. The charge transfer resistance (R_{ct}) gives an indication of the reaction speed in kinetically regulated reactions. The lower this number is, the easier it is to transmit charge and the faster the reaction takes place. [20]

1.4.5 Faradaic Efficiency (FE)

Faradaic efficiency, which measures how effectively electrons supplied by an external circuit participate in HER, is a crucial metric to assess the performance of an electrocatalyst. The ratio of the experimental to the theoretical amount of hydrogen generation is known as Faradaic efficiency in HER. The amount of hydrogen theoretically

from faradays law (1.14) using parameters obtained from galvanostatic or potentiostatic electrolysis conditions.

$$FE = \frac{nNF}{Q} \times 100 \% \quad (1.14)$$

n is the number of electrons exchanged in the faradaic process, Q denotes the total charge transmitted during the entire reaction, and N denotes the amount of H_2 produced in moles.

1.4.6 Turnover Frequency (TOF)

The intrinsic site activity or site efficiency of an active catalyst candidate for a process of interest is commonly determined by the number of active sites per weight or volume of the catalyst when evaluating and screening it against competing catalysts. The total number of molecules changed into the desired product per catalytic site per time unit is known as the turn over frequency (TOF). It is calculated from

$$TOF = \frac{I}{2Fn}$$

Where I is the measured current (A), F is Faraday constant and n is the number of moles of the active catalyst. [21]

1.5 Electrocatalysts For Hydrogen Evolution Reaction

Due to their optimum hydrogen binding energy and Gibbs free energy for atomic hydrogen adsorption, along with low activation energies for H desorption from the surface, platinum group metal-based catalysts and their derivatives have emerged as the most efficient

catalysts for HER, delivering exceptional exchange current density (j_0) close to the thermodynamic potential, small Tafel slope as well as 100% Faradaic efficacy.[22] However, the high cost of platinum group metals and inadequate stocks on Earth limit the widespread use of platinum group metal-based catalysts to create H₂ on a scale commensurate to global energy consumption.[19] Recently, a lot of effort has been put into finding earth-abundant electrocatalysts with high activity, cheap, and good stability. The fundamental principle underlying the development of electrocatalysts depends on two aspects; increasing the number of active sites can be achieved by tuning the catalyst's morphology, porosity, and specific surface area and by boosting intrinsic activity by heteroatom doping, interface construction, and defect management. As a result, many transition metal-based catalysts, including metal alloys, metal oxides, metal sulfides, metal phosphides, metal selenides, metal nitrides, metal carbides, and metal-free catalysts, including heteroatom-doped nanocarbon materials, polymers, and their composites, were investigated as catalysts for different electrocatalytic reactions.[23]-[28] Among these, catalysts with porous architectures usually display improved catalytic activity because of more exposed catalytic sites and higher suitable containment for active species. To this end, Porous Organic Polymers (POP) represent ideal porous structures due to their ability to incorporate several catalytically active species within their frameworks.[29]

1.6 Porous Organic Polymers (POPs) for HER

Porous organic polymers (POPs) are a type of multi-dimensional porous network material made up of strong covalent bonds between organic building blocks of varied morphologies and topologies having extended 2D or 3D architectures. According to their structural characteristics, they can be categorized as amorphous or crystalline. Hyper-crosslinked polymers (HCPs), polymers of intrinsic microporosity (PIMs), conjugated microporous polymers (CMPs), and porous aromatic frameworks (PAFs) are examples of amorphous POPs, whereas covalent organic frameworks (COFs) are examples of crystalline POPs[30]. Their pores, which IUPAC classifies according to their widths as micropores (less than 2 nm), mesopores (2–50 nm), and macropores (more than 50 nm), define a material's internal surface area. The relative ease and accurate tunability of POPs to achieve the desired composition, porosity, stability, and functionality is advantageous for electrocatalytic site exposure, substrate or product diffusion kinetics, and transfer of electrons on the overall framework, allowing POPs to be used as electrocatalysts for the HER. POPs used in the HER can be classified into heteroatom-containing POPs and metalized POPs.

1.6.1 Heteroatom-containing POPs

The synthesis of naturally containing hetero-atom (B, C, O, F, P, and S) rich polymers or post-synthetic non-metal doping, in particular, has been established as a vital way of improving the electrocatalytic performance of porous polymers. Ball et al. investigated the change in HER performance of Si and P co-doped bipyridine-linked covalent triazine

framework (CTF) by replacing the bipyridine hydrogens with fluorine atoms (SiPF-Bpy-CTF) using density functional theory (DFT). They discovered that SiPF-Bpy-CTF, after co-doping and substitution, has a narrow band gap (7 meV) and a great GH value close to 0 eV, which may allow it to achieve optimal charge transfer kinetics during the HER.[31]

Porphyryns are heterocyclic conjugated aromatic molecules with high nitrogen content, made up of four pyrrole subunits linked together by methyne bridges. The porphyrin's aromatic conjugated structure allows for rapid electron transport during the electrocatalytic reaction. Patra et al. reported a metal-free containing porphyrin covalent organic polymer (TpPAM) that contains nitrogen which can operate as an active core for electrocatalytic HER. The conjugation and heteroatom abundance offered the polymer easy charge transfer at the electrode-electrolyte interface, showing a charge transfer resistance of 90.34 Ω displayed and requiring only 250 mV to achieve a current density of 10 mAcm⁻². [32] Using Schiff base reaction of 5,10,15,20-tetrakis(4-aminophenyl) porphyrin (TAP) with 1,3,6,8-tetrakis(4-formylphenyl)pyrene (TFFPy), Pradhan and co-workers developed a pyrene-porphyrin containing imine-based COF (SB-PORPy). Due to the N-content, π -electronic conjugation, and pyrene-induced π - π stacking interaction, SB-PORPy shows a Tafel slope of 116 mVdec⁻¹ for the HER in 0.5 M H₂SO₄. [33] Furthermore, Wang et al. compared the charge transfer effectiveness between 2D and 3D N-containing POPs. They found that 2D N-rich covalent quinazoline network (TQ-CQN) exhibits a lower charge transfer when compared to a 3D N-rich POP based on tricycloquinazoline. TQ-CQN has a low Tafel slope of 40 mVdec⁻¹ when used as the catalyst for the HER, demonstrating its quicker

kinetics, which is mainly due to its fully conjugated rigid plane and ordered π - π array stacking.[34]

1.6.2 Metal Encapsulated POPs

The wide acceptability of Metal-based materials for HER electrocatalysis has made metalation of POPs a well-known promising technique for increasing activity by increasing the number of active sites in POPs. The condensation of metallated octahydroxyprophyrin with squaric acid produced a bimetallic (Co and Ni) enclosed 2D porphyrin polymer, according to Ranjeesh and colleagues. This metalloporphyrin-based 2D sheet exhibits exceptional catalytic performance for the hydrogen evolution reaction, with a faradaic efficiency of 97%, an overpotential of 105 mV at a current density of 10 mA cm⁻², and a Tafel slope of 74.1 mVdec⁻¹. The porous structure and inclusion of Ni ions in the Co framework are primarily responsible for the improved HER performance.[35] In another study, the Schiff base condensation process and subsequent coordination with Co(II) were used to create a Co-porphyrin-based covalent organic polymer (CoCOP). Faster adsorption and desorption of reaction intermediates on/from CoCOP leads to improved HER kinetics because the frontier orbital energy of CoCOP is altered due to the efficient charge transfer from the Co porphyrin moiety to imine groups.[36] Khaligh et al. described a novel Ni functionalized covalent organic framework (COF-TPP-CB[6]) that was built by clicking perpropargyloxy cucurbit[6]uril (CB[6]) to azido-functionalized tetraphenylporphyrin (TPP-4N3) via a copper-catalyzed azide-alkyne cycloaddition reaction (CuAAC). Using electrochemically active porphyrin cores as building blocks and multi functionalities like

triazole and carbonyl groups that may coordinate with the metal cocatalyst (Ni), they loaded a small amount (12 %) of Ni to the framework, thereby showing a remarkable H₂ production rate of 18.7 mmol h⁻¹g⁻¹ and a modest starting potential of 250 mV.[37]

1.7 Porous Organic Polymers for Supercapacitors

In terms of power density and energy density, supercapacitors have been shown to be critical bridges between regular capacitors and batteries. Compared to traditional electrolytic capacitors, they have a substantially higher energy density. Despite having a lower energy density than batteries, supercapacitors can store and transmit large amounts of energy in seconds, giving them a higher power density than batteries.[38] They can be divided into two types based on the working principle; electrochemical double-layer capacitors (EDLC) and pseudo capacitors.[39] The adsorption of electrolyte ions on the vast surface area of conductive porous electrodes determines the energy storage mechanism of EDLCs. It does not involve a redox reaction. According to a recent study, EDLC performance is influenced by specific surface area, pore diameters, pore connectivity, wettability, and carbon nanostructures. In pseudo capacitors, energy is stored by reversible surface redox processes at the electrolyte/electrode interface. Although pseudo capacitors have a high capacitance and energy density, they have poor cycling stability and have a low power density. Carbon materials such as porous carbons, carbon nanotubes, graphene, transition metal oxides, transition metal sulfides, molecules with O- and N-containing surface functional moieties, and conducting polymers are commonly utilized for this purpose.[39]

Porous organic polymers involving covalent organic frameworks (COFs) and amorphous conjugated micro-/mesoporous polymers (CMPs) have stood out due to their adjustable pore sizes, large surface area, and controllable functionalities, making them rather appealing candidates as electrode material for energy storage applications. Li et al. synthesized DBT-MA-COF (figure 1-2), a two-dimensional triazinyl porous organic framework produced through a C–N coupling reaction using 2,5-dibromothiophene and melamine as reaction monomers. The high heteroatom content of the material was utilized to facilitate the rapid transfer of electrolyte ions and improved solution conductivity. When used with Nitrogen-doped chitosan-derived carbon material to assemble an asymmetric supercapacitor, the electrode delivered a high energy density of 32.1 W h kg^{-1} and power density of 800 W kg^{-1} , retaining 83 % efficacy even after 30,000 cycles of galvanostatic charge discharge[40]. Similarly, Patra et al. used the Schiff base condensation procedure to make a benzimidazole-based covalent-organic polymer with a high capacitance of 335 Fg^{-1} and good cyclic stability of up to 1000 cycles.[41] Furthermore, Bhanja et al. synthesize a COF, TDFP-1, by combining two monomers, 1,3,5-tris(4-aminophenyl)triazine and 2,6-diformyl-4-methylphenol, in a Schiff base condensation reaction. With a pair of redox peaks emerging from the COF, a superior capacitance of 354 Fg^{-1} at 2 mVs^{-1} was attained, along with good capacitance retention.[42]

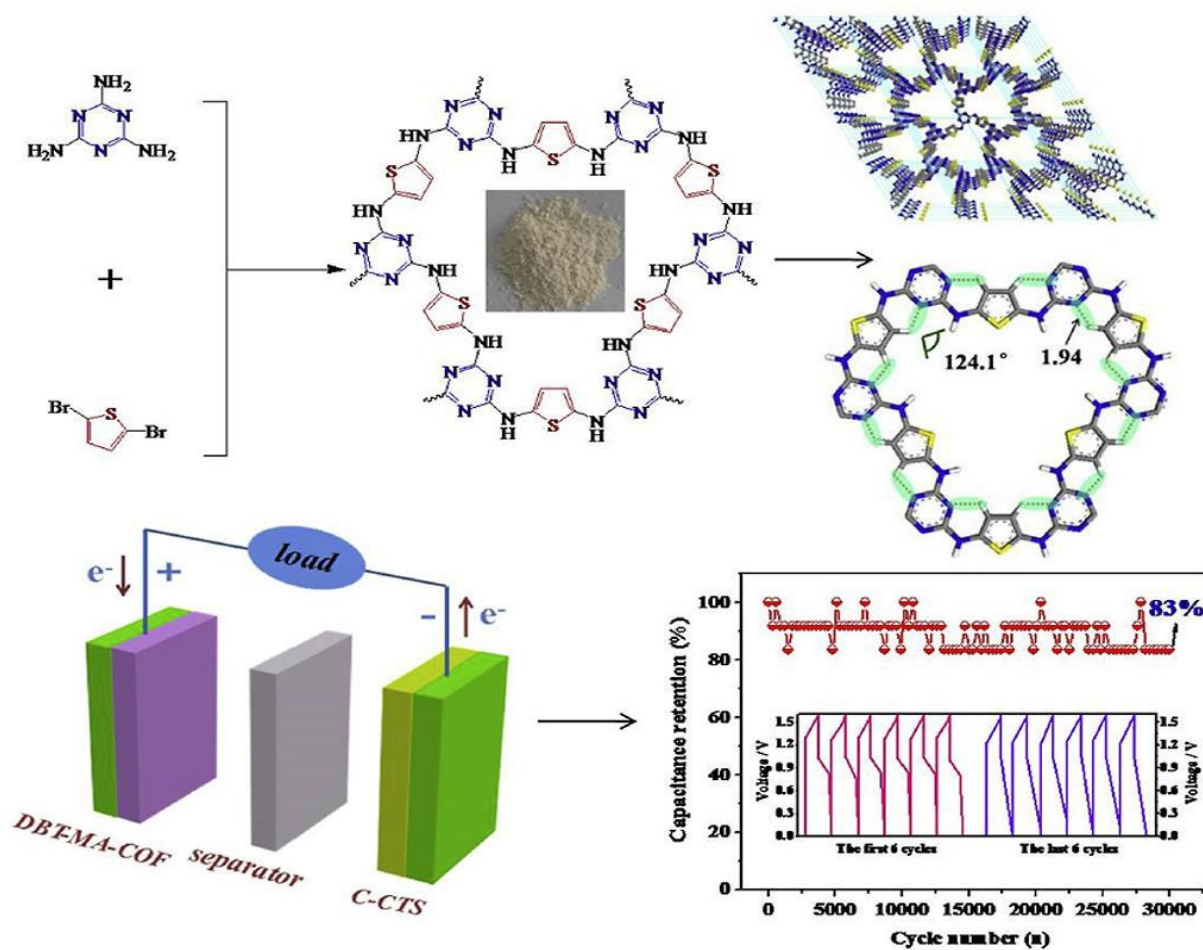
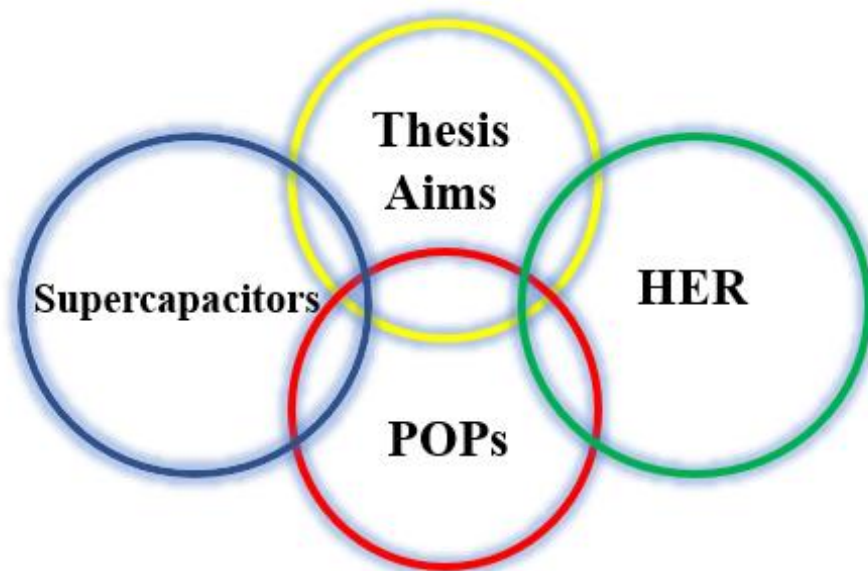


Figure 1-2: Illustration of synthesis of DBT-MA-COF and its electrochemical performance. Reprinted from ref [40] Copyright (2021), with permission from Elsevier.

1.8 Aim of The Study



The main topic of this research focuses on the utilization of melamine-based microporous organic polymer (MOP) in electrochemical hydrogen production. The effect of encapsulation of different weight ratios of Ni on the electrocatalytic activity of the polymer is investigated. The synthesis and characterization of MOP using scanning electron microscope (SEM), x-ray photoelectron spectroscopy (XPS), x-ray diffraction (XRD), uv-vis spectroscopy, Fourier-transform infrared spectroscopy (FTIR), transmission electron microscopy (TEM), thermogravimetric analysis (TGA) and nitrogen adsorption measurement is initially discussed. For hydrogen evolution reaction (HER), electrolyte optimization is carried out by investigating the pristine MOP in acidic, basic, and neutral solutions. Following optimization, further studies looked at the effects of varying Ni weight ratios on the HER performance of the catalyst. The optimum Ni functionalized electrode's

robustness for HER electrocatalysis was finally proven by the retention of its morphology and chemical composition in the post-catalytic SEM and XPS analysis respectively. To our knowledge, this is the first study on employing pyrolysis-free Ni encapsulated microporous organic polymer built from melamine and thiophene organic building blocks as an electrocatalyst for hydrogen production.

The second part of the study briefly introduces the application of porous organic polymer, and cucurbituril-derived porous carbon material as electrode materials for supercapacitors.

CHAPTER 2

EXPERIMENTAL AND INSTRUMENTATION

2.1 Chemicals

All chemicals, reagents and solvents used throughout this study were of analytical grade and used as received with no further purification unless otherwise stated. 2,5-thiophenedicarboxaldehyde (Th), melamine (Me), nickel acetate tetrahydrate, acetone, tetrahydrofuran, dichloromethane, dimethyl sulfoxide (DMSO), potassium hydroxide (KOH), sulfuric acid (H_2SO_4 , 95-97%), phosphate buffered saline (PBS), and platinum on carbon (Pt/C) were purchased from Sigma-Aldrich. Boron trifluoride diethyl etherate ($\text{BF}_3 \cdot \text{Et}_2\text{O}$) and Nafion (5% w/w in water and 1-propanol) were purchased from Alfa Aesar. Ultrapure deionized water ($R \geq 18 \text{ M}\Omega \text{ cm}^{-1}$) from a Milli-Q plus water purification system (Millipore, Bedford, MA, U.S.A.) was used when required.

2.2 Synthesis

The microporous organic polymer was synthesized via a one-pot polycondensation reaction as follow: 2,5-thiophenedicarboxaldehyde (200 mg, 1.44mmol) and melamine (180mg, 1.43mmol, 1eq.) were added in 5 ml DMSO. After ultrasonic dissolution at room temperature, 15 μl of the catalyst, $\text{BF}_3 \cdot \text{Et}_2\text{O}$, was added to the solution. The reaction mixture was refluxed overnight at 140 °C under N_2 atmosphere. After the completion of

reaction, (by the attenuation of the strong carbonyl peak in FT-IR), the resulting solution was cooled to room temperature. MOP was precipitated as a brown solid after adding 40 ml acetone which was subsequently filtered and washed with dichloromethane, tetrahydrofuran, and hot methanol to remove the unreacted monomers. The product was finally dried in a vacuum oven at 100 °C for 4 h. Yield: 330 mg (86 %).

2.3 Structural Determination and Characterization Techniques

Before using in electrochemical analysis, the microporous organic polymer (MOP) was all characterized using the available instrumentation techniques. The best electrochemical activity sample was then chosen, and it was further characterized using SEM, TEM, XPS, and FT-IR.

2.3.1 Scanning Electron Microscope

A scanning electron microscope (SEM) is a type of electron microscope that produces images of a sample by scanning it with a focused beam of electrons. The secondary and backscattered electrons are detectable and carry details about the sample's surface topography and composition due to the electrons' interactions with the atoms in the sample. FEIQuanta 200 FEG ESEM was employed to analyze the surface topology and composition of a sample material. Additionally, the EDX analysis system was used to analyze the elemental mapping and composition of specimens.

2.3.2 X-ray Photoelectron Spectroscopy

The MOP's elemental composition, empirical formula, chemical state, and electronic state can all be determined using the quantitative spectroscopic method known as X-ray photoelectron spectroscopy (XPS). A typical XPS spectrum represents the number of observed electrons vs. their binding energy. Each element directly identifies itself as existing in or on the surface of the sample material by producing a distinctive collection of XPS peaks at unique binding energy values. Using a Thermo Scientific K-Alpha X-Ray Photoelectron Spectrometer system with an AlK α monochromator source operating at 400 mm spot size and $h\nu=14.866$ eV along with a flood gun for charge neutralization, 200 eV for survey scan, and 30 eV for individual scans, the surface chemistry and identity of chemical bonds in the sample were examined. All binding energies were calculated by referencing the carbon support's C1s spectra, 284.6 eV.

2.3.3 X-ray Diffraction

A non-destructive X-ray diffraction analysis (XRD) method can provide precise information on a material's crystallographic structure, chemical makeup, and physical characteristics. To gather a variety of crystallographic data, X-ray diffraction (XRD) uses the coherent scattering of X-rays by crystalline materials. This thesis investigated the crystalline structure using the XPert Pro Multipurpose X-ray Diffractometer (MPD). CuK X-Ray radiation ($= 1.5418$ Å) with a 2θ diffraction angle range of 4-80°, step size of 0.05, and time per step of 500s was used to perform the XRD experiments.

2.3.4 Infrared Spectroscopy

The interaction of a single beam of non-dispersed IR radiation with a sample is recorded by an FT-IR spectrometer, which measures the frequencies and intensities of the absorptions. Functional groups in chemicals have been found to absorb light at specific frequencies. Consequently, the recorded frequencies can be used to establish the chemical structure. Attenuated Total Reflectance – Fourier Transform Infrared Spectroscopy (ATR FT-IR) recorded by Bruker Alpha Platinum-ATR spectrometer model was used to further analyze the functional groups and bonds present in the MOP. 64 scans in the wavenumber range of 400–4000 cm^{-1} were used to record the spectra in transmission mode.

2.3.5 UV-VIS Spectroscopy

Diffuse Reflectance Absorption (DRA) spectra were recorded with Agilent Cary 5000 UV–vis–NIR spectrophotometer with spectral bandwidth down to 0.2 nm and Xenon Flash Lamp as the light source. The UV-Vis absorbance of the samples was recorded in solid state within the range 200-800 nm.

2.3.6 Transmission Electron Microscopy

A beam of electrons is carried through an incredibly thin specimen using the microscopy technique known as transmission electron microscopy (TEM), interacting with the material as it does so. The interaction of the electrons passing through the material results in the formation of an image, which is magnified and focused onto an imaging device. FEI Tecnai G2 F30 TEM was used to investigate the sample morphology and structure further.

2.3.7 Thermogravimetric Analysis

Thermogravimetric analysis (TGA), a technique for thermal analysis, measures how the mass of materials change as a function of temperature (while maintaining a constant heating rate). TGA measurement was done on TA Instruments Q500 thermogravimetric analyzer at a heating rate of 10 °C/min from 25 °C to 900 °C.

2.3.8 Nitrogen Adsorption Measurement

During N₂ adsorption measurement, a sample is exposed to N₂ gas at various pressures and the liquid-nitrogen temperature, -196 °C. Increased pressure causes more N₂ molecules to become adsorbed on the sample's surface. The amount of N₂ gas adsorbed is calculated using the universal gas law after measuring the pressure at which adsorption equilibrium is reached. As a result, an adsorption isotherm is established. The pressure is then gradually reduced to cause the adsorbed N₂ molecules to desorb, producing a desorption isotherm. Information regarding the sample's pore structure, including specific surface area, pore-volume, and pore size, can be obtained by analyzing the adsorption and desorption isotherms in conjunction with some physical models such as the Brunauer-Emmett-Teller (BET) model. In this thesis, the sample's N₂ adsorption and desorption isotherms were determined at -196 °C using a Quantachrome autosorb iQ surface area and pore size analyzer. Before the analysis, the samples were degassed under a vacuum at 90 °C for 24 h. The value of P/P₀ was increased from 0.080 to 0.985 and subsequently reduced to 0.14 for determining the adsorption/desorption isotherm.

2.4 Preparation of Working Electrodes

2.4.1 Hydrogen Evolution Reaction

The working electrode was prepared by gently grinding 5 mg of the as-synthesized MOP with various mass ratios of nickel acetate tetrahydrate salt (1:0.25, 1:0.5, 1:1, and 1:2). Then, 300 μl deionized water, 70 μl ethanol, and 15 μl nafion were added to the ground powder, and the mixture was stirred overnight at room temperature. Finally, 20 μl of the as-prepared ink was drop-casted over the conductive side of clean FTO glass ($2\times 1\text{ cm}^2$), covering a $1\times 1\text{ cm}^2$ area. The catalyst-coated FTO electrodes were dried overnight under ambient conditions.

2.5.2 Supercapacitors

The working electrode was prepared by gently grinding the active materials (MOP and CB[6]-porphyrin framework), activated carbon and polyvinylidene fluoride (PVDF) binder in the proportion of 80:10:10 mass ratio. An appropriate amount of N-Methylpyrrolidone (NMP) was added and mixed to form a uniform slurry mixture. The slurry was then uniformly applied using a brush to the stainless steel (SS304) used as a collector with a mass loading of about 1 mg and vacuum-dried at 80 $^{\circ}\text{C}$ for 2 hours.

2.5 Electrochemical Measurement

All electrochemical measurements (for HER) were performed using a CHI608E potentiostat at room temperature in a conventional three-electrode cell configuration with silver/silver chloride ($\text{Ag}/\text{AgCl}/\text{KCl}_{(\text{sat.})}$), spiral Pt wire, and catalyst-coated fluorine tin

oxide (FTO) as the reference (RE), counter (CE), and working electrodes, respectively. Before the electrode coating, the FTO substrates were cleaned by washing them with water and soap, followed by ultrasonication in deionized water and isopropanol each for 10 min. Then, they were activated in a furnace at 450 °C for 45 min. Before each measurement, the electrolyte solution was saturated with argon gas (99.999% of purity) for 30min.

CHAPTER 3

RESULTS AND DISCUSSION

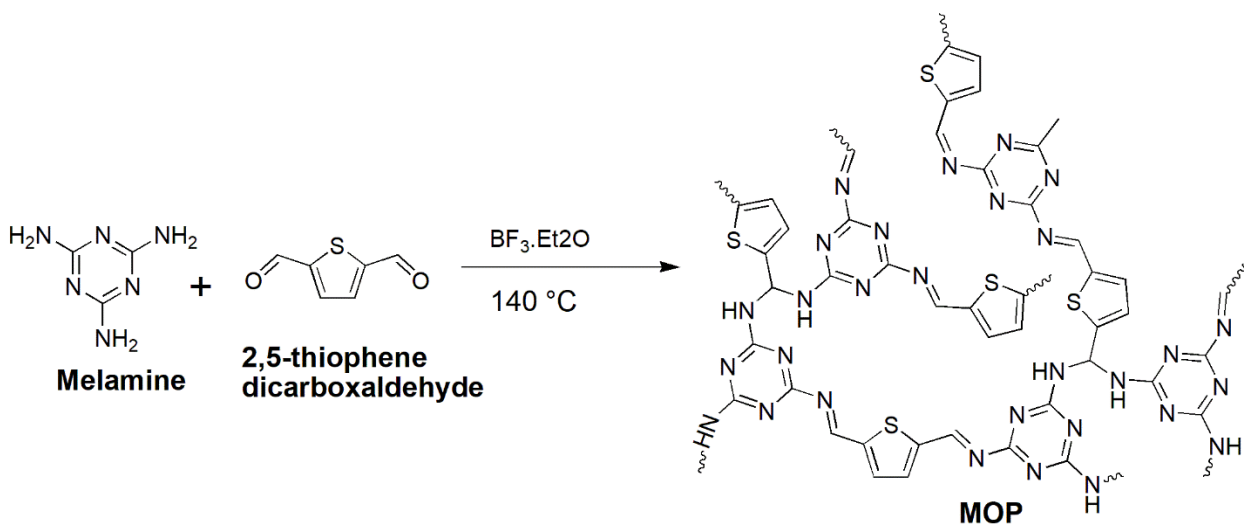
3.1 Section 1: Microporous Organic Polymer (MOP) for Hydrogen Evolution Reaction

The synthesis and characterization of the microporous organic polymer are described at the outset of this section. A series of electrochemical measurements were then carried out, and its electrochemical behavior toward HER was examined in acidic, basic, and neutral electrolytes. After selecting the best electrolyte solution in terms of catalytic activity and durability, these techniques were used to conduct the electrochemical measurements. Next, the effect of incorporating nickel salt into the framework was investigated, and it was discovered that the electrocatalytic behavior of the MOP significantly improved. The mechanism of Ni coordination is then explained. The optimal electrode was thoroughly characterized by scanning electron microscopy, and X-ray photoelectron spectroscopy before and after the electrochemical measurement.

3.2 Synthesis and Characterization of MOP

The synthetic route of the proposed MOP is detailed in Scheme 1. Imine bonds were initially created when melamine reacted with 2,5-thiophendicarboxaldehyde through the Schiff base reaction, a condensation process involving the nucleophilic addition of primary amines and active carbonyl groups. The primary amines then attack the imine bonds,

leading to the production of polyamines. The reaction started as a clear solution and gradually turned black before producing many precipitates (after adding acetone) and producing brown agglomerated particles as the end result of MOP. MOP is hyper-cross-linked, as evidenced by its insolubility in water and many routinely used organic solvents, including methanol, tetrahydrofuran, dichloromethane, and dimethyl sulfoxide.[43]



The FT-IR Spectra of the MOP compared with its monomers, melamine (Me), and 2,5-thiophenedicarboxaldehyde (Th), were shown in Figure 3-1. A series of peaks at 1556 cm^{-1} , 1441 cm^{-1} , and 1346 cm^{-1} belong to the triazine unit. After polymerization, the strong attenuation of the carbonyl stretching signal (-C=O- , 1651 cm^{-1}) from 2,5-dicarboxaldehyde of thiophene and -NH_2 band of melamine (1610 cm^{-1}) as well as the appearance of the stretching vibration of secondary amine (-N-H- , 3341 cm^{-1}) in the FT-IR spectrum of MOP compared to Th and Me monomers indicates the success of the polycondensation reaction.

The peak at 812 cm^{-1} belongs to C-S stretching signal of thiophene rings. The slight stretching peak around 1650 cm^{-1} corresponding to the imine (C=N) group is identified in the FTIR spectrum of MOP, proving that not all imine bonds are reduced in the build-up to the formation of the polyaminal network.[44],[45] Diffuse reflectance ultraviolet-visible (UV-vis) spectroscopy of both thiophene monomer and MOP (Figure 3-2) exhibited a broad and strong absorption band in the visible region. However, the apparent redshift tendency of MOP may be attributed to extended conjugation, further indicating the existence of some imine units in the framework. On the other hand, a noticeable narrow absorption band was observed in the UV-vis spectra of Me and physical mixture of monomers, clearly indicates that the MOP is only formed through the polycondensation reaction between the monomers.[46]

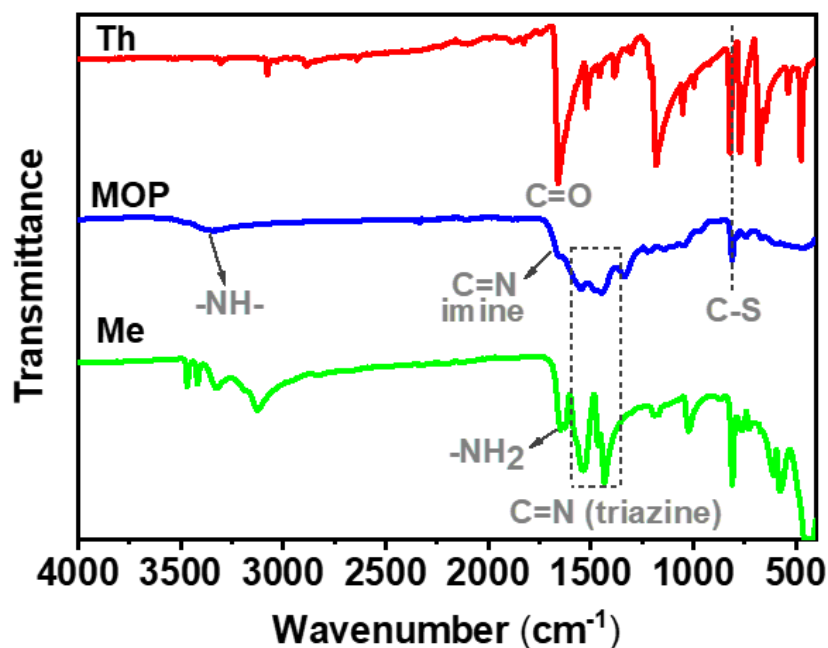


Figure 3-1: FT-IR spectra of MOP compared to its monomers, melamine (Me), and 2,5-thiophenedicarboxaldehyde (Th).

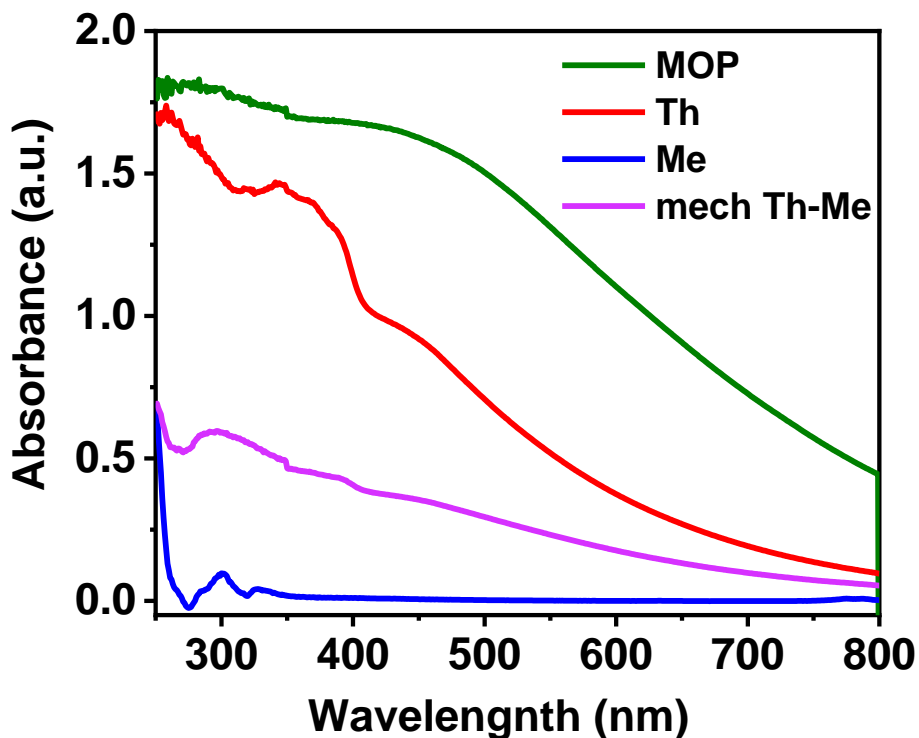


Figure 3-2: UV spectrum of MOP, its monomers, and the mechanical mixture of the monomers

By using XPS analysis, the chemical and elemental makeup of the MOP was investigated (Figure 3-3). The XPS data further support the FT-IR spectra showing the surface binding sites of the porous polymer. The six fitted components in Figure 3-3a corresponds to C1s XPS spectrum of MOP, which stand for the bonds C=C, C-C, C-S, C-N-C, C=N, and N-C=N, respectively, are 284.28, 284.88, 285.38, 285.78, 286.48, and 287.88 eV. Figure 3-

3b shows the deconvoluted N1s XPS spectra with two peaks at 398.88 and 400.28 eV corresponding to the C-N=C of the triazine and the C-N of the aminal bond, respectively.[47] Similarly, the S2p spectrum (Figure 3-3c) can be fitted into two peaks at 163.98 eV ($2p_{3/2}$) and 165.08 eV ($2p_{1/2}$), corresponding to the C-S-C bond.

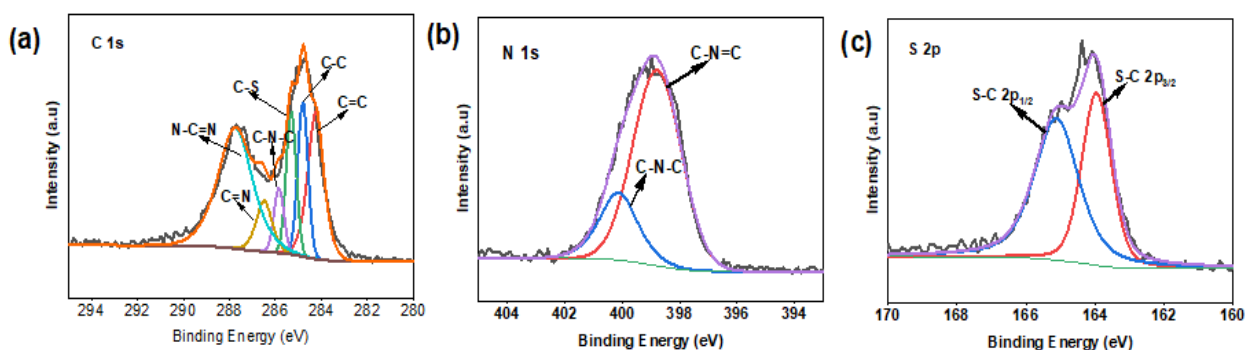


Figure 3-3. High resolution XPS spectra of (a) C 1s, (b) N 1s (c), and S 2p for **MOP**

The morphology of the MOP was examined by SEM and TEM imaging. The SEM image (Figure 3-4a) shows that the structures are based on a cotton-like morphology with particle agglomerations similar to reported microporous polymers.[48] A closer study of TEM images (Figure 3-4b) further confirmed the porous and agglomerated morphology of the MOP. Figures 3-4c and 3-4d show the SEM/EDX elemental mapping for the distribution of C, N, and S in the MOP, as well as the associated EDX spectrum and atomic proportion of elements.

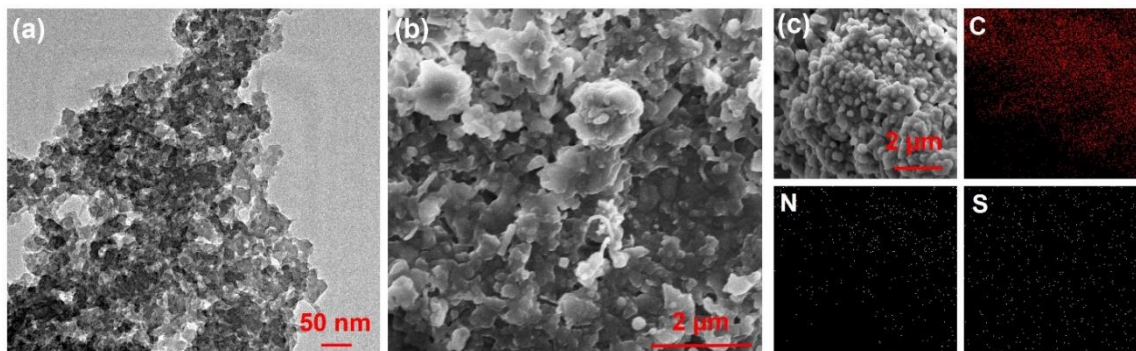


Figure 3-4: (a) TEM; (b) SEM Images ;(c) Elemental Mappings; (d) SEM/EDX spectrum of MOP and the corresponding atomic percentage of elements; of Pristine MOP

A single, distinctive diffraction peak at $2\theta = 23.1^\circ$, which can be attributed to the (001) plane of the regularly ordered lattice and suggests interlayer-stacking, was visible in the powder XRD pattern of the MOP (Figure 3-5a). The broadness of the peak, on the other

hand, denotes small crystal size and uneven layer stacking. Figure (3-5b) illustrates how the XRD spectrum of MOP validates its amorphous character, which is very distinct from the crystalline structure of its monomers. [49][50]

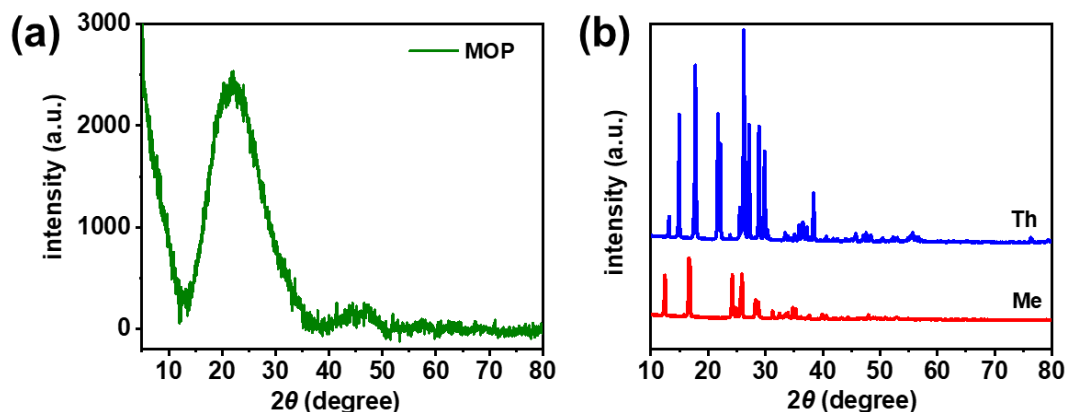


Figure 3-5: (a) XRD spectrum of MOP; (b) XRD spectrum its monomers

To assess the specific surface area and porous nature of the as-synthesized MOP, the N_2 adsorption-desorption isotherm was performed at $-196\text{ }^{\circ}\text{C}$. The adsorption isotherms (Figure 3-6) revealed an abrupt gas uptake at low relative pressures and a flat course in the middle. There is no hysteresis during desorption. This resembles a type I isotherm, which indicates that the polymer network is microporous[51], according to the IUPAC classification. The sample's Barrett–Joyner–Halenda (BJH) total specific pore volume and Brunauer–Emmett–Teller (BET) specific surface area were calculated to be $0.047\text{ cm}^3\text{ g}^{-1}$ and $195.731\text{ m}^2\text{ g}^{-1}$, respectively. As a result, the BJH pore size distribution curve (Figure 3-7), with pore diameter and radius of 1.53 nm and 3.73 nm, indicated microporous distribution.

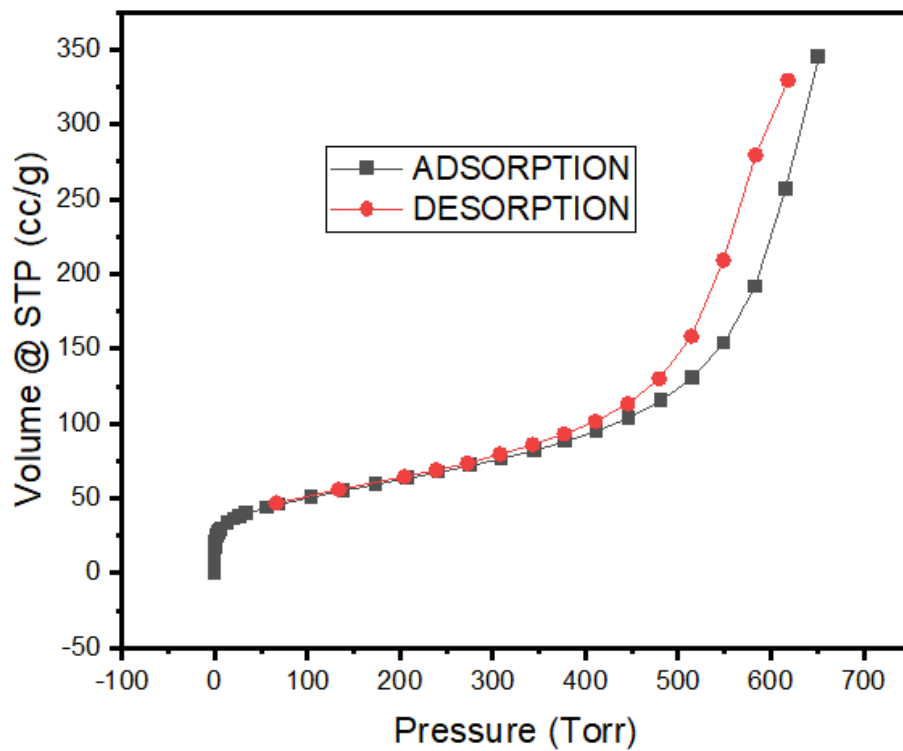


Figure 3-6: N₂ physisorption isotherm of MOP.

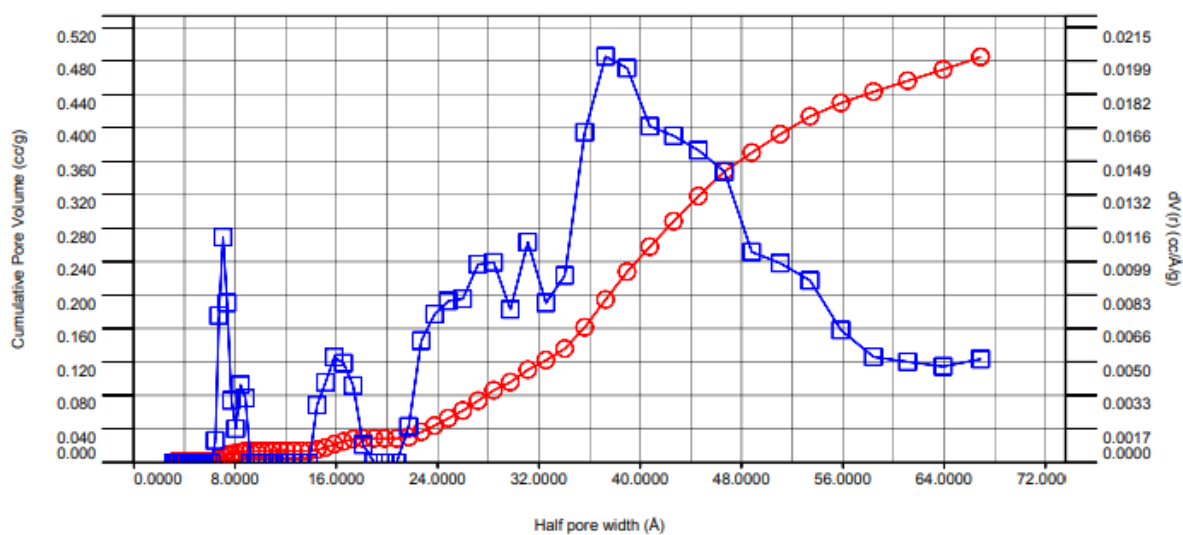


Figure 3-7: BJH pore size distribution of MOP

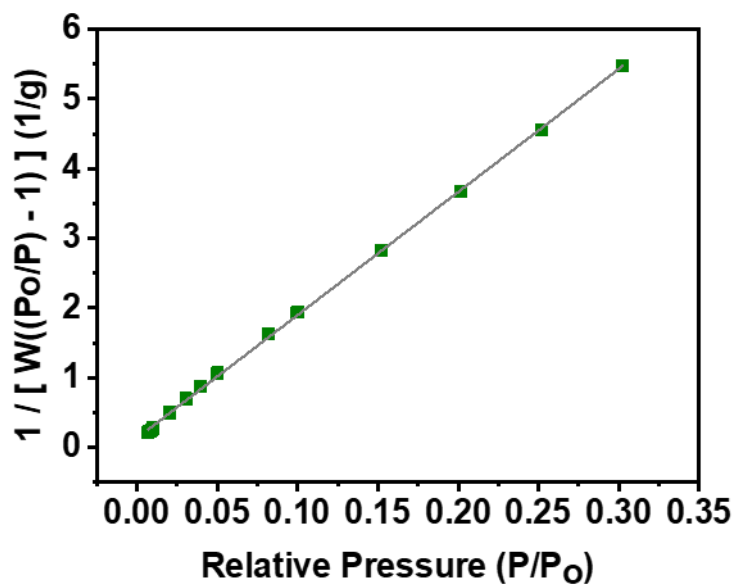


Figure 3-8: Multipoint BET of MOP ($R^2= 0.9999$).

The TGA technique (figure 3-9), used in a nitrogen environment from 25 to 900 °C with a heating rate of 10 °C min⁻¹, was used to examine the thermal stability of the MOP network. Three deterioration stages were visible in the MOP sample. The physically adsorbed water and solvent molecules trapped inside the polymer network are responsible for the first negligible weight loss (4%) below 200 °C. Melamine units started to lose considerable amounts of weight (25.5%) at about 300 °C, and weight loss above 550 °C can be attributed to the degradation of the polymer network. Additionally, at this third stage, a post-polycondensation process could occur where water is released when the polymer end groups (-NH₂ and -CHO) continue to react[52]. The comparison of the TGA curves of MOP and its monomers was also exhibited in Figure 3-9. It can be seen the individual monomers are significantly unstable over the 900 °C temperature range, with over 95 %

weight loss around 400 °C. However, MOP showed remarkable stability, losing only around 30 % at 400 °C and an overall weight loss of 80 % at 25-900 °C.

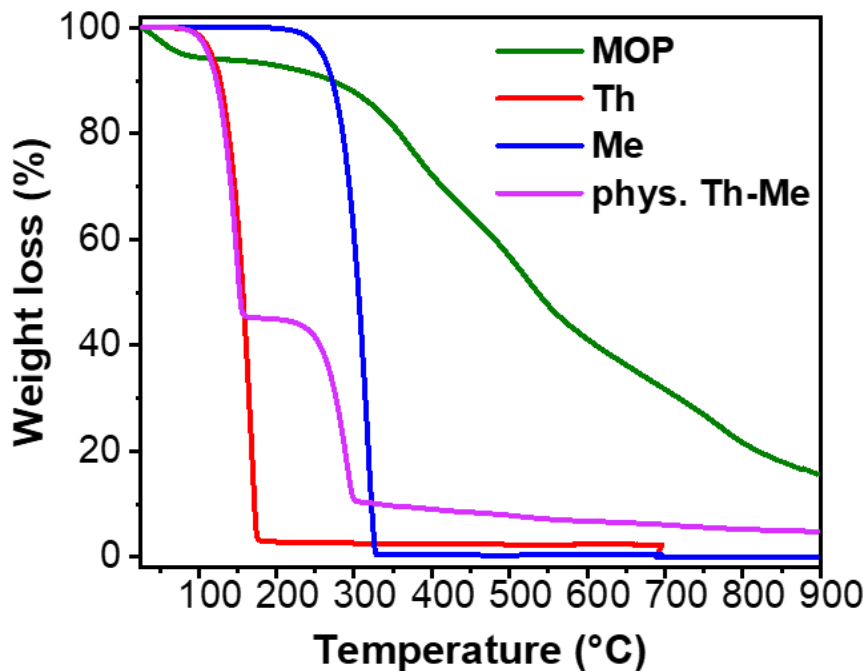


Figure 3-9: TGA graph of MOP, its monomers and mechanical mixture of the monomers

3.3 Evaluation of Electrocatalytic HER Activity of MOP

After carrying out the MOP's comprehensive characterization, its HER electrocatalytic performance was then examined. The heteroatom content and multiple functions of the melamine and thiophene building blocks produce a unique electronic structure with strong conductivity and excellent charge mobility and provide coordinating sites for non-precious nickel co-catalyst and quickly transport electrons during the HER, are here the key

characteristics of the MOP. The framework's excellent electrochemical activity is the result of these synergistic processes, which also increase energy transfer efficiency.

In this context, using linear sweep voltammetry (LSV) at a scan rate of 10 mVs^{-1} under Ar-saturated conditions, the electrocatalytic HER performance of the pristine MOP was initially examined in various electrolytes including acidic ($0.25 \text{ M H}_2\text{SO}_4$), neutral (0.1 M PBS), and basic (0.1 M KOH and 0.5 M KOH) solutions. All LSV graphs showed increased cathodic current with a particular negative bias. An abrupt increase in cathodic current signaled the beginning of HER on the catalyst-coated FTO (covered area $1 \times 1 \text{ cm}^2$) electrode surface. The sample LSV curves of the geometric current density (mA cm^{-2}) vs. applied potential are shown in Figure 3-10a. Based on the Nernst equation, all observed potentials are related to a reversible hydrogen electrode (RHE).

Despite having onset potentials of $+254 \text{ mV}$ and -240 mV , respectively, the MOP sample deteriorated and peeled off in electrolytes of $0.25 \text{ M H}_2\text{SO}_4$ and 0.1 M PBS after the first measurement. However, the electrode endured numerous LSV tests in basic media. Although the catalyst in this case has a lower onset potential in 0.1 M KOH (-326 mV) than in 0.5 M KOH (-410 mV), overpotentials of -800 mV and -679 mV are still needed to achieve the current density of 10 mAcm^{-2} in 0.1 M KOH and 0.5 M KOH , respectively. Additionally, in 0.5 M KOH , the electrode showed a more significant overall current density than in 0.1 M KOH , reaching up to 35 mAcm^{-2} . Therefore, 0.5 M KOH electrolyte was used for all electrochemical investigations.

By grinding 5 mg MOP with 1.25, 2.5, 5, and 10 mg nickel acetate tetrahydrate salt during the ink production process, as previously detailed in Section 2.4.1, nickel was loaded as a co-catalyst to enhance the HER electrocatalytic performance of MOP in the optimum alkaline medium. Four distinct electrodes were created by altering the nickel concentration: Ni_{0.25}@MOP, Ni_{0.5}@MOP, Ni₁@MOP, and Ni₂@MOP. This was done to study the impact of the nickel content on the HER performance of the Ni@MOP electrocatalyst (the subscripts indicate the weight ratios of nickel acetate salt with respect to MOP). The best experimental conditions were used to perform the LSV measurements on all Ni@MOP electrodes, and the polarization curves obtained were compared to those of pristine MOP and 10 % Pt/C as shown in Figure 3-10b. It is important to note that the HER overpotential (η) indicates the effectiveness of the electrocatalyst and provides an idea of the level of polarization that happens when Faradaic current flows through it (due to HER). A lower value indicates that an electrocatalyst has better catalytic activity for efficient H₂ production with a modest cathodic bias. The effectiveness of a HER catalyst is determined by the overpotential needed to provide a current density of 10 mAcm⁻². [53]

In this situation, Ni was added to the MOP to create Ni_{0.25}@MOP, which drastically modified the MOP's activity by causing the onset potential to change from -415 mV to a more positive value of -343 mV and increasing the cathodic current density. Due to a potential mismatch between the active sites of the parent catalyst and the Ni co-catalyst, a modest decrease in onset potentials was seen as the Ni concentration was raised in the Ni_{0.5}@MOP electrode. Of the four Ni composites, Ni₂@MOP showed the highest HER

performance overall and had the most favorable onset potential at -66 mV (Figure 3-10b). Additionally, only 17 mV more negative than the present standard of 10% Pt/C was needed for the optimum to achieve a current density of 10 mA cm⁻² (-580 mV) (Figure 3-10c), a value that is quite comparable to several other HER electrocatalysts. The electrocatalytic HER performance of the composite electrodes improved in the order of Ni_{0.5}@MOP < Ni₁@MOP < Ni_{0.25}@MOP < Ni₂@MOP. After 90 % manual ir-correction (Figure 3-10d inset), The $\eta@10mAcm^{-2}$ for Ni₂@MOP and 10 % Pt/C reduced to -470mV and -428mV, respectively. Figures 3-11a and 3-11b show the manually adjusted ir-polarization curves for Ni₂@MOP and 10 % Pt/C, respectively. The better catalytic performance of the composite with the highest Ni content suggests that the synthesized MOP is a useful template for metal ion encapsulation.

The Tafel plot provides a more thorough understanding of the electrochemical proton reduction process at the catalyst surface. A lower Tafel slope value is related to faster electrode kinetics. Exchange current density (ECD, i_0), which is proportional to the rate of an electrochemical reaction, is another important kinetics measure from the Tafel plot. The ECD value increases as the electrochemical process quicken. Here, by plotting overpotential versus log (current density), the Tafel plots of the investigated electrocatalysts were produced (Figure 3-10d) from the linear section of the respective LSV polarization curves. The highest Tafel slopes were demonstrated by Ni_{0.5}@MOP and Ni₁@MOP, at 251 mVdec⁻¹ and 262 mVdec⁻¹, respectively. Ni₂@MOP displayed the lowest Tafel slope of 212 mVdec⁻¹ among the composites implying that it is the composite

with the fastest kinetics, consistent with the results from the polarization curves and comparable with existing non-precious metal electrocatalyst in literature.[54] For ECD, Ni_{0.5}@MOP had the lowest value (0.390mAcm⁻²) which is closely followed by Ni₁@MOP (0.392mAcm⁻²) and Ni_{0.25}@MOP (0.397mAcm⁻²). Ni₂@MOP electrocatalyst produced the highest exchange current density (0.439mAcm⁻²), confirming its superior electrode kinetics to the corresponding composites, as shown in table 3-1.

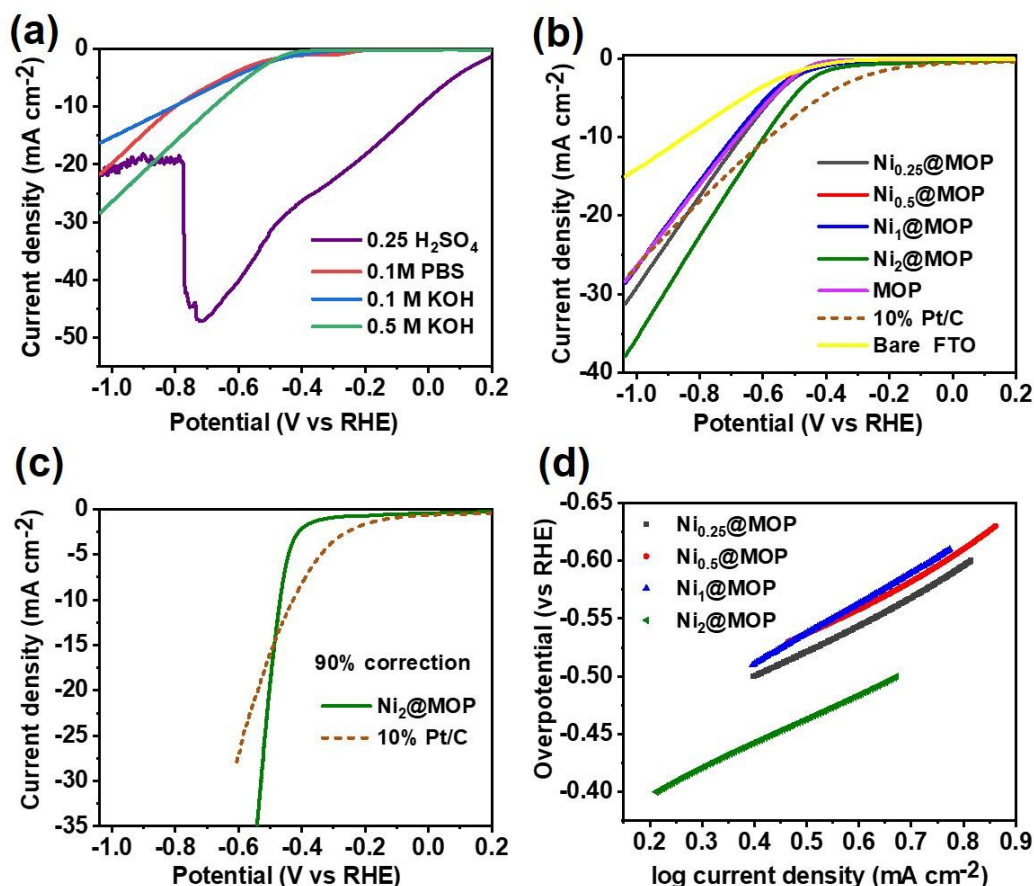


Figure 3-10 (a) LSV polarization curves for pristine MOP at 10 mVs⁻¹ in different electrolytes (b) LSV polarization curves of Ni@MOP catalysts with varying Ni content in comparison with bare FTO and standard 10% Pt/C, measured at 10 mVs⁻¹ in 0.5 M KOH,

(c) Tafel plots obtained from the linear region of LSV, and (d) The iR-corrected LSV curve of the optimum $\text{Ni}_2\text{@MOP}$ catalyst compared to the standard 10% Pt/C measured at 10 mVs^{-1} in 0.5 M KOH.

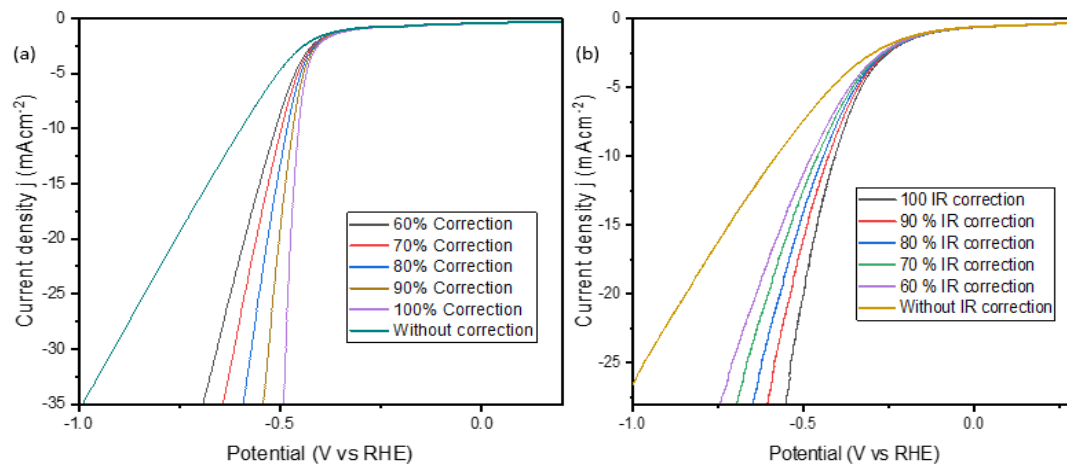


Figure 3-11: (a) Polarization curves of $\text{Ni}_2\text{@MOP}$ with and without manually IR correction
(b) Polarization curves of 10 % Pt with and without manually IR correction

Table 3-1: Electrochemical parameters of the various electrocatalysts investigated towards HER in 0.5 M KOH

Sample	Onset (mV)	$\eta@10\text{mAcm}^{-2}$ (mV)	Tafel Slope (mVdec⁻¹)	i_0 (mAcm⁻²)	J @ $\eta = -0.597\text{ V}$ (mA cm⁻²)	TOF (s⁻¹)
Ni_{0.25}@MOP	-343	-668	-239	0.397	-6.396	0.0737
Ni_{0.5}@MOP	-351	-685	-251	0.390	-5.505	0.0385
Ni₁@MOP	-327	-693	-262	0.392	-5.111	0.0235
Ni₂@MOP	-66	-597	-212	0.439	-10.000	0.0345
MOP	-415	-679	-244	0.395	-6.093	-

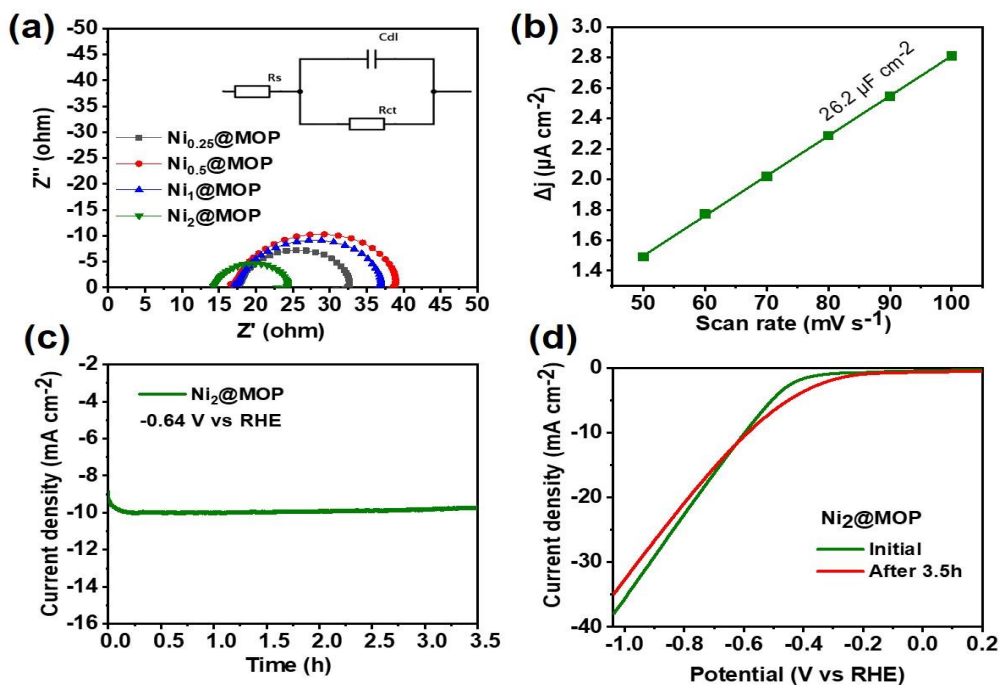
A technique called electrochemical impedance spectroscopy (EIS) was utilized to analyze the samples' interfacial charge transfer resistance. The experiments were conducted between 0.1 Hz and 10 kHz in 0.5 M KOH at -0.64 V against RHE. Figure 3-12a displays the Nyquist curve for the various Ni@MOP samples. The diameter of the semicircle arc in the Nyquist plot represents the charge-transfer resistance (R_{ct}) of the electrode-electrolyte interface. It was found that the R_{ct} values of the Ni composites decreased in the following

order: Ni_{0.5}@MOP > Ni₁@MOP > Ni_{0.25}@MOP > Ni₂@MOP. The R_{ct} value of the Ni₂@MOP electrode was 10.01, which is better than those previously reported HER electrodes.[55][56] A straightforward Randles equivalent circuit model can be used to simulate the electrochemical performance of Ni₂@MOP (Figure 3-12a inset). The Ni₂@MOP material's low charge-transfer resistance demonstrated its quick electronic transport capabilities, which led to a potent electrocatalytic activity. The optimum sample's swift charge transfer capacity may be due to the extended conjugated electronic structure of the organic building blocks and the Ni co-catalyst. The absence of a diffusion-limited electrochemical reaction on the electrode surface was confirmed by the absence of Warburg impedance in the low-frequency zone.[32] The resistance values obtained for Ni@MOP catalysts were listed in Table 3-2.

By performing a series of cyclic voltammetry (CV) experiments in the non-faradaic area of 0 to 0.1 V vs Ag/AgCl at various scan rates from 50 to 100 mVs⁻¹, the double-layer capacitance (C_{dl}) of the ideal Ni₂@MOP catalyst was determined (figure 3-12b and 3-12e). The Ni₂@MOP sample's C_{dl} value was discovered to be 26.2 μFcm⁻², indicating a more significant amount of electrochemically active surface area (ECSA) that may cause the sample's increased electrocatalytic activity.

When assessing the catalyst's potential for practical use in water splitting, stability is a crucial consideration. Chronoamperometry (CA) experiment was used to examine the stability of the ideal Ni₂@MOP electrocatalyst at a constant potential of -0.64 V vs. RHE in 0.5 M KOH (Figure 3-12c). The Ni₂@MOP electrode demonstrated adequate stability

for 3.5 h with negligible current loss throughout the testing time, leading to a faradaic efficiency of 92.78 % in the first hour, 92.04 % in the second hour, and 90.84 % in the third hour, indicating that the Ni₂@MOP catalyst's ability to produce hydrogen remained unaltered. Additionally, the Ni₂@MOP's LSV polarization curve, which was recorded after a 3.5-hour durability test, was essentially unaltered, demonstrating its excellent stability and outstanding HER performance in an alkaline medium (Figure 3-12d).



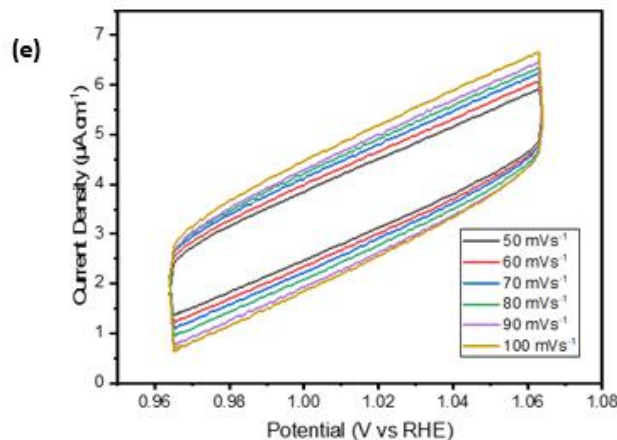


Figure 3-12: (a) The Nyquist plots of various Ni@MOP catalysts recorded at -0.64 V vs RHE in 0.5 M KOH (b) The capacitive currents (Δj) at 1.02 V vs RHE as a function of scan rate for Ni₂@MOP catalyst in 0.5 M KOH ($\Delta j = j_{anodic} - j_{cathodic}$), (c) chronoamperometry of Ni₂@MOP under constant potential of -0.64 V vs RHE in 0.5 M KOH, and (d) the corresponding polarization curves of Ni₂@MOP before and after chronoamperometry obtained at 10 mVs⁻¹ in 0.5 M KOH. (e) CV of Ni₂@MOP at different scan rates

Table 3-2: R_u and R_{ct} Values for Ni@MOP Samples

Sample	R_u (Ω)	R_{ct} (Ω)
Ni _{0.25} @MOP	17.73	14.92
Ni _{0.5} @MOP	16.57	22.30
Ni ₁ @MOP	17.09	19.73
Ni ₂ @MOP	14.24	10.01

3.4 Pre- and Post-Catalytic Characterization of Ni₂@MOP

Utilizing XPS and FTIR, it was determined if the Ni cocatalyst was successfully coordinated in the ideal sample, Ni₂@MOP. Figure 3-13a illustrates a comparison of the FTIR spectra of Ni₂@MOP with the pristine MOP. The mechanism of Ni co-catalyst coordination with the pristine MOP involves synergistic effects of coordination interaction (between electron donor moieties with electron-accepting heavy metal ions) and electrostatic interaction (between the electron bearing negatively polarized functional groups and positively charged metal ions). Due to its interactions with the highly ordered triazine nitrogen atom and thiophene sulfur atom via electrostatic and chelation interactions, the nickel ion has two potential coordination modes. From the FTIR spectra of the Ni loaded MOP catalyst, a bathochromic shift of the triazine stretching vibration peaks from 1558cm⁻¹ and 1540cm⁻¹ to 1531 cm⁻¹ and 1520cm⁻¹, the secondary amine stretch from -NH- from 3360 cm⁻¹ to 3124 cm⁻¹, and the C-S peak from 812 cm⁻¹ to 750 cm⁻¹ clearly confirms the Ni ion coordination.[57] The high-resolution XPS profile of the N 1s, S 2p, and Ni 2p region validated the binding relationship between the metal co-catalyst, triazine moiety, and the sulfur atom. The presence of Ni²⁺ can be demonstrated by the high-resolution Ni 2p region (Figure 3-13c), where typical peaks at 856.78 and 874.18 eV can be assigned to Ni 2p_{3/2} and Ni 2p_{1/2} electronic configurations, respectively.[58] The subpeak at 853.18 eV can be assigned to the Ni-S bond.[59] The N 1s (Figure 3-13b) can be fitted into three peaks with Ni-N located at 397.58 eV. In addition to the subpeaks in the S 2p spectrum of the pristine MOP (Figure 3-3c), a strong peak appeared at 169.28 eV

in the S 2p region of the Ni₂@MOP (Figure 3-13d).[60][61] The notable intensity of this new peak indicates stronger interaction between the sulfur atom and the Ni ion.

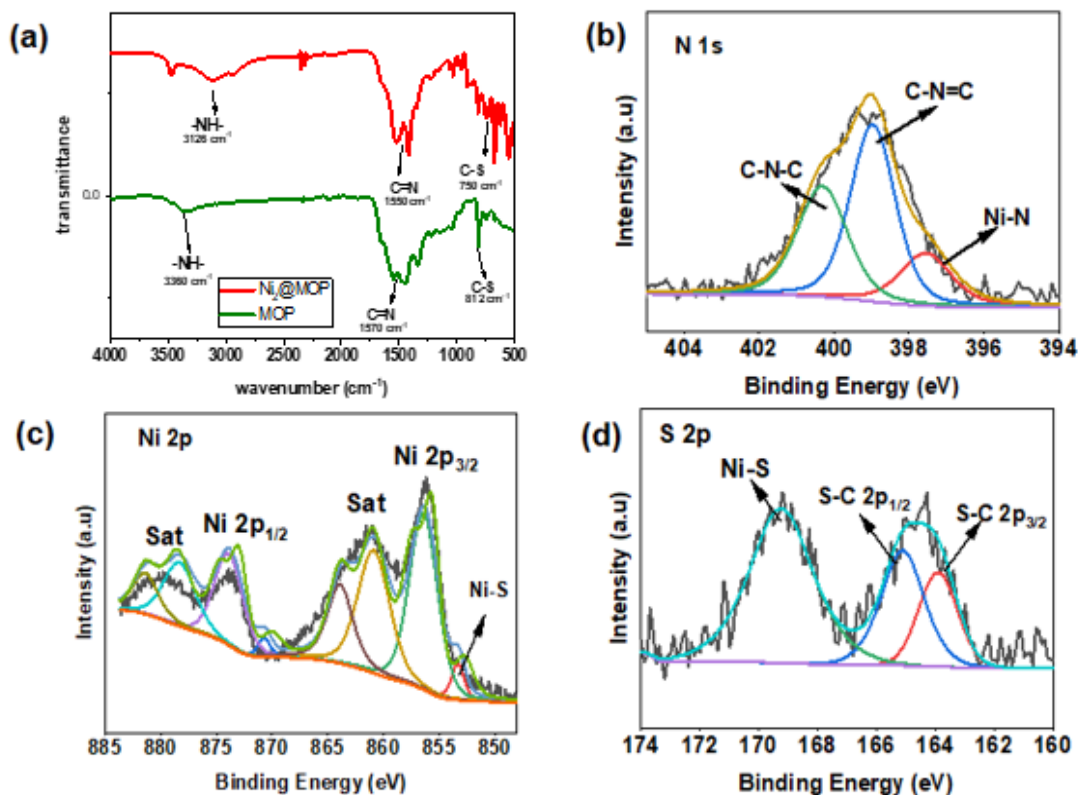


Figure 3-13: (a) FTIR spectrum of pristine MOP and Ni₂@MOP; High resolution XPS (b) N 1s (c) Ni 2p (d) S 2p for Ni₂@MOP

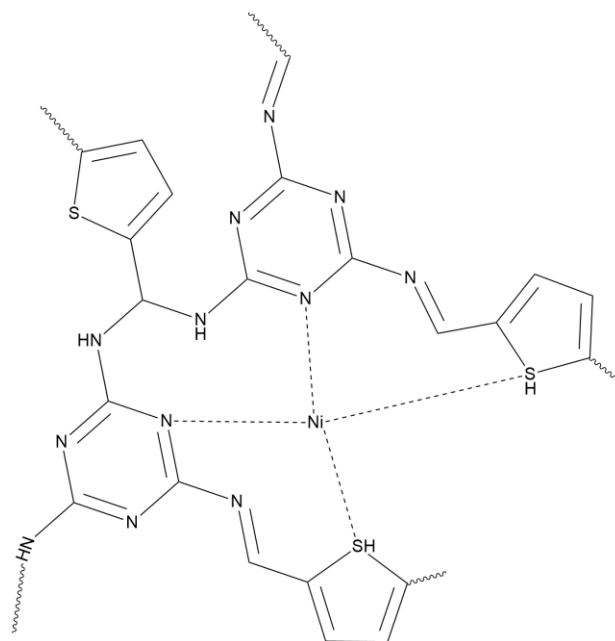


Figure 3-14: Proposed Ni mechanism of interaction with MOP

Also, TEM image of Ni₂@MOP is shown in figure 3-15, with the dark spots confirming the encapsulation of the nickel co-catalyst.

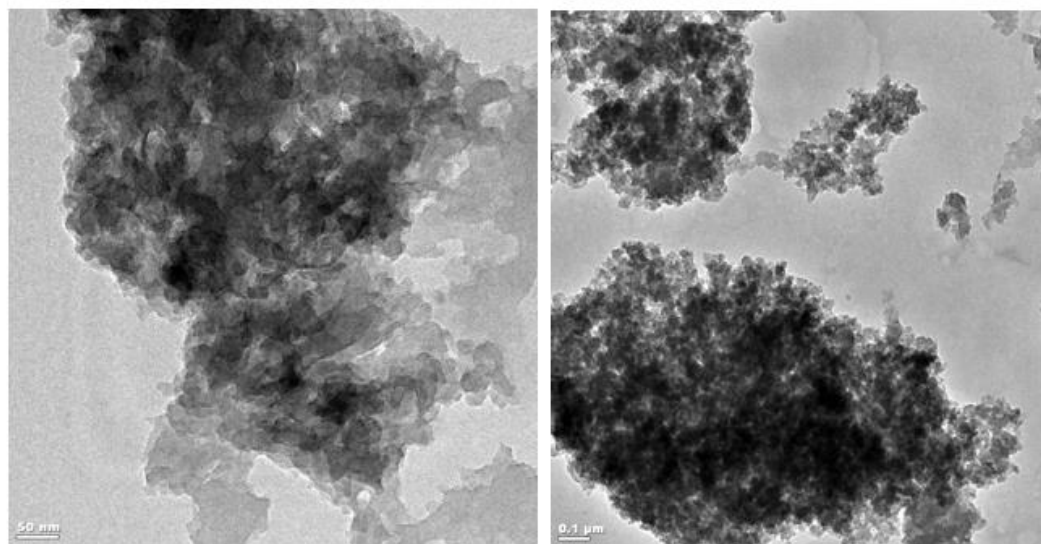


Figure 3-15: TEM images of Ni₂@MOP

The Ni₂@MOP electrode was characterized with SEM/EDX and XPS after the durability test utilizing the CA experiment. According to SEM (Figure 3-16) and EDX elemental mapping, the electrode's morphology was the same before and after the CA experiment. Similarly, the electrocatalyst did not change significantly and maintained its chemical composition, as seen by the high-resolution XPS spectra of Ni₂@MOP before and after the 3.5 h CA experiment (Figure 3-17). The Ni²⁺ spectrum fitted into seven peaks were assigned to Ni 2p_{3/2}, Ni 2p_{1/2}, their satellites, and Ni-S. The peaks around 856.78, which can be assigned to Ni 2p_{3/2}, and the corresponding satellite peaks at 861 and 864 eV remain essentially unchanged. The main peak around 874.18 eV, and the peaks at 878.48 and 881.4 eV assigned to Ni 2p_{1/2} electronic configurations, and its satellites were similarly intact. The subpeak at 853.18 eV belonging to the Ni-S bond was also not significantly altered, corroborating the chemical robustness of the catalyst for HER.

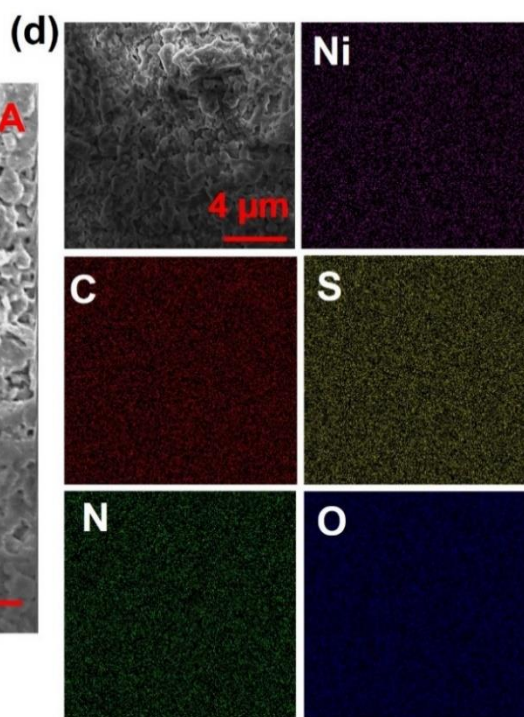
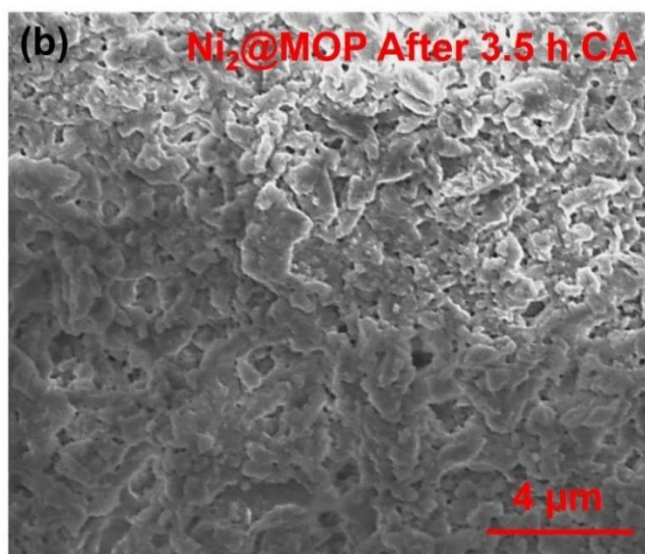
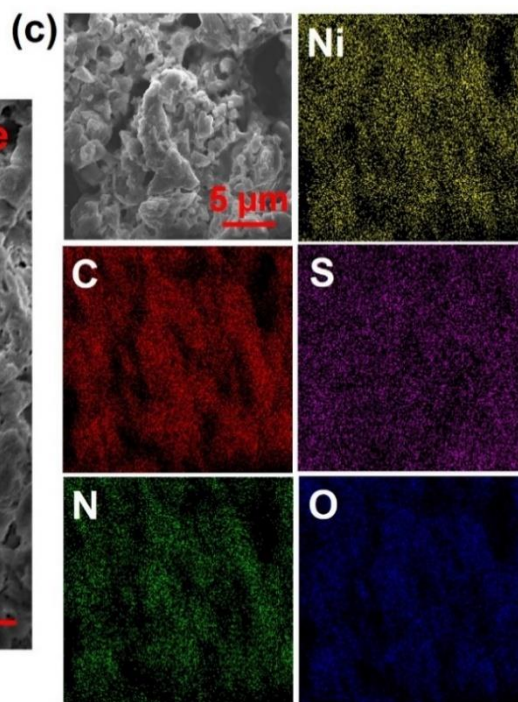
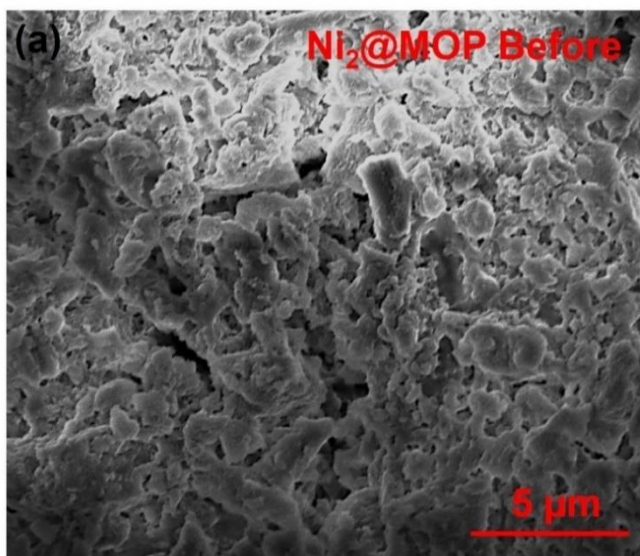
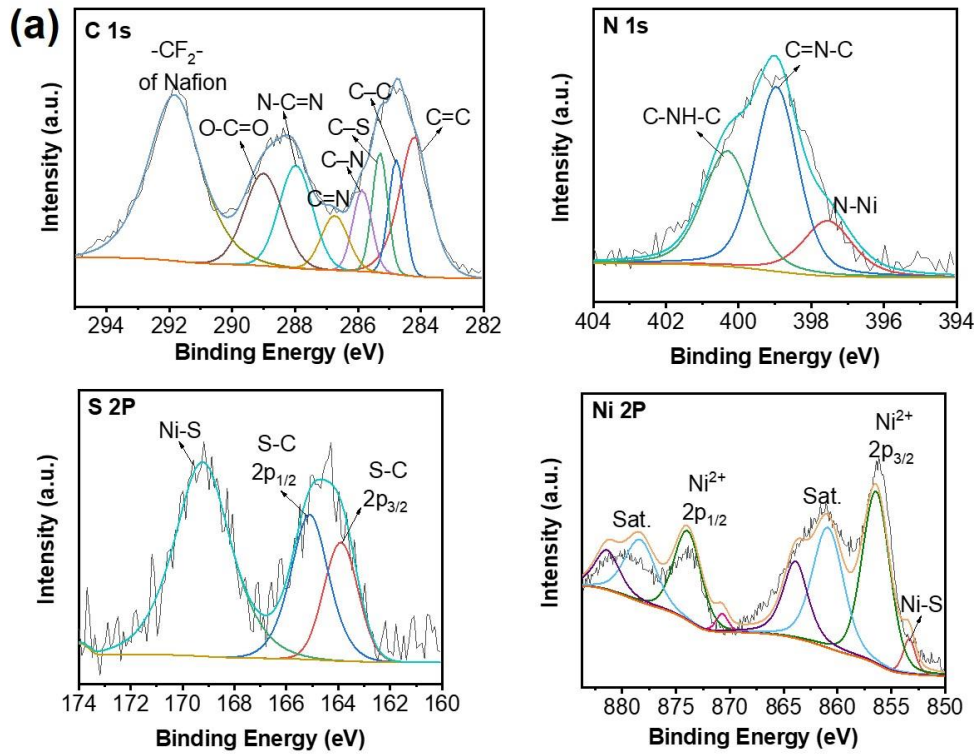


Figure 3-16: SEM images of Ni₂@MOP (a) before and (c) after 3.5 h chronoamperometry experiment at -0.64 V vs. RHE in 0.1M KOH, (b, d) corresponding elemental mapping images of elements C, N, O, S, and Ni



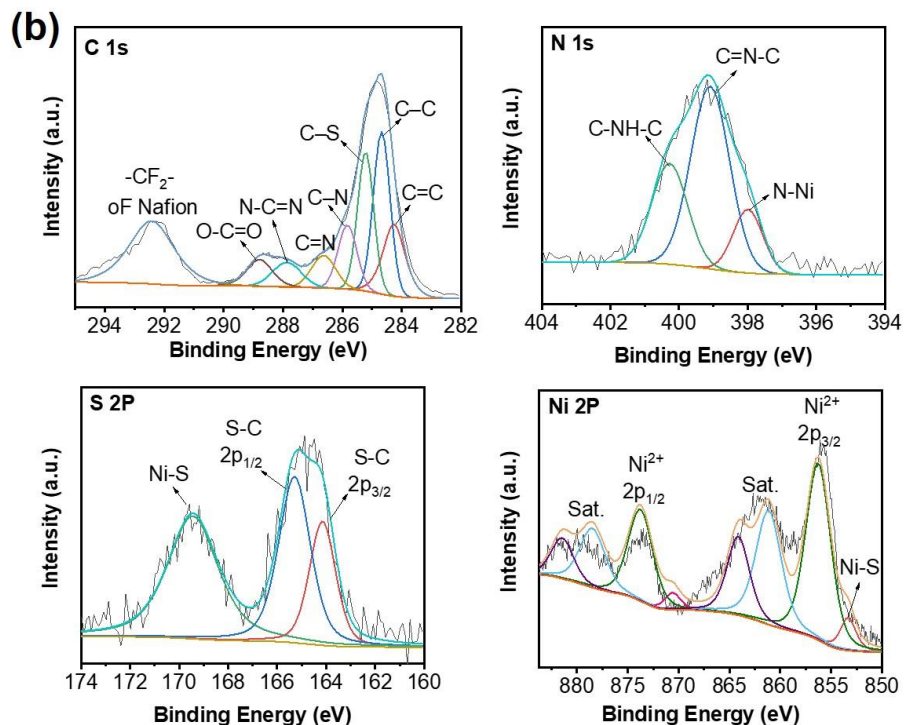
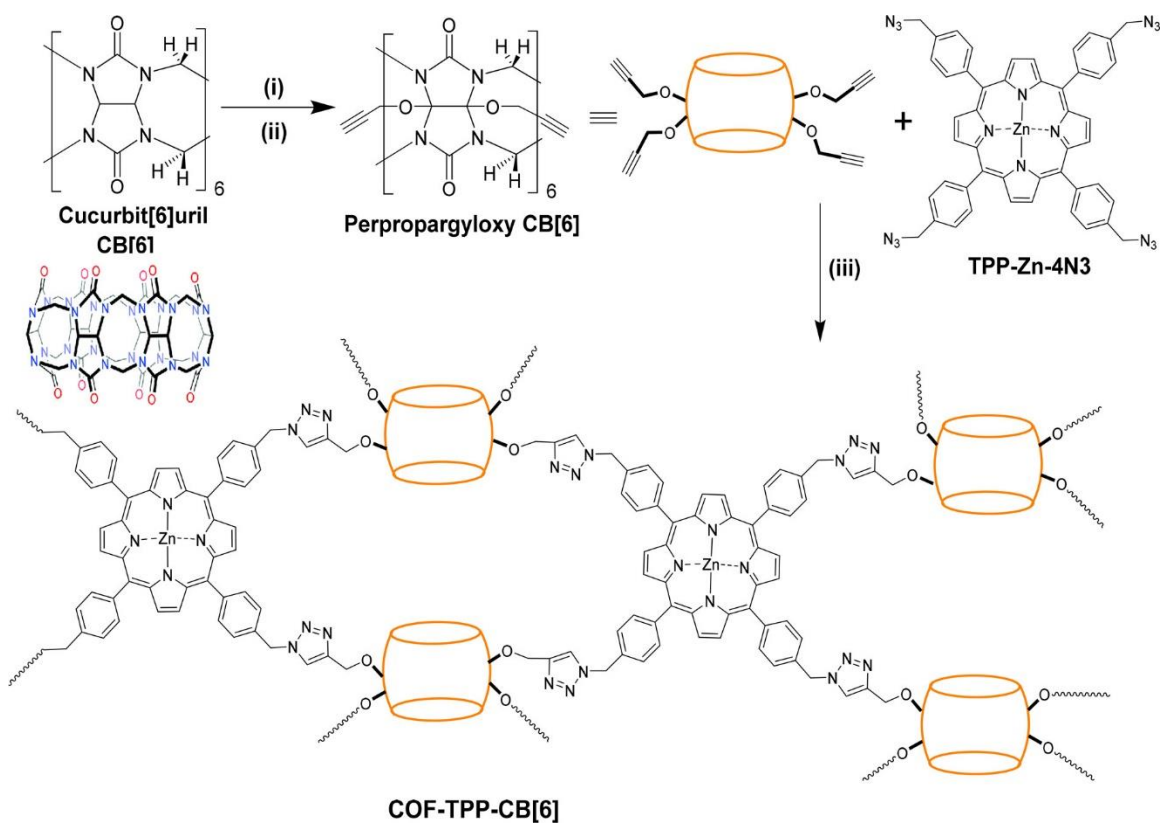


Figure 3-17: XPS data of Ni₂@MOP (a) before and (b) after 3 h chronoamperometry experiment at -0.64 V vs. RHE in 0.5M KOH

3.5 Section 2: Porous Organic Polymers as Electrode Materials for Supercapacitors

In this section, a brief report on the evaluation of the melamine-based microporous organic polymer (MOP) and porphyrin-cucurbit[6]uril covalent organic framework (CB[6]-porphyrin framework) as electrode materials for supercapacitor energy storage is presented. The MOP has a significant heteroatom concentration since the material's structure contains triazine units and thiophene units, which will facilitate the transfer of electrolyte ions through its channels, making them potentially suitable for use as the

supercapacitor energy storage. The CB[6]-porphyrin framework has been synthesized through copper-catalyzed azide-alkyne cycloaddition reaction (Cu-AAC) as depicted in Scheme 3-2 and utilized by our group members (Aisan Khaligh and Yasaman Sheidaei) for hydrogen production. The presence of multifunctionalities (carbonyl, imine), high heteroatom content, and the electrochemically active porphyrin core made the CB[6]-porphyrin framework a potential candidate for application as supercapacitor electrode.[37]



Scheme 3-2: Synthesis of **COF-TPP-CB[6]**: (i) $K_2S_2O_8$, H_2O , $85\text{ }^\circ\text{C}$, 6 h, N_2 ; (ii) NaH , Dry $DMSO$, Propargyl Bromide, $25\text{ }^\circ\text{C}$, Overnight, N_2 ; and (iii) $DMSO$, Copper Sulfate/Sodium Ascorbate, $120\text{ }^\circ\text{C}$, 96 h. "Reprinted with permission from [37]. Copyright {2021} American Chemical Society."

3.5.1 Evaluation as Electrode Materials for Supercapacitors

Using cyclic voltammetry and chronopotentiometry techniques, the materials were evaluated in a conventional 3-electrode cell. The working electrode was prepared by gently grinding the active materials (MOP and CB[6]-porphyrin framework), activated carbon and polyvinylidene fluoride (PVDF) binder in the proportion of 80:10:10 mass ratio. An appropriate amount of N-Methylpyrrolidone (NMP) was added and mixed to form a uniform slurry mixture. The slurry was then uniformly applied using a brush to the stainless steel (SS304) used as a collector with a mass loading of about 1 mg and vacuum-dried at 80 °C for 2 hours. Silver/silver chloride (Ag/AgCl/KCl_(sat.)) and spiral Pt wire were used as a reference and counter electrodes in 6M KOH aqueous electrolyte solution.

Figures 3-18a and 3-18b displayed the cyclic voltammetry (CV) curves of MOP and CB[6]-porphyrin framework at the potential window of -1–0 V and 0-0.6 V vs Ag/AgCl respectively. They are nearly rectangular, which indicates that the electrodes are effectively propagating charges.

The potential windows of -1-0 V and 0-0.7 V were used to measure the MOP and CB[6]-porphyrin framework electrodes for the galvanostatic charge-discharge (GCD) test (Figures 3-19a and 3-19b). The following formula was used to get the specific capacitance (C) of the GCD curve for various current densities:

$$C = \frac{I \times \Delta t}{m \times \Delta V}$$

Δt = Discharge time (Sec) from GCD study

ΔV = Potential window (V)

I = Constant current used for charging and discharging (mA)

m = mass loading of the active material (mg)

At the current density of 0.1 mA g^{-1} , MOP displayed a specific capacitance of only 0.9 F g^{-1} . On the other hand, CB[6]-porphyrin framework displayed significantly lower current density and GCD measurement was only possible at 0.001 mA g^{-1} , giving a specific capacitance of 0.038 F g^{-1} . These results are substantially poorer than those reported for porous organic polymers. T. Li et al reported a stable benzobisthiazole-linked covalent organic framework having a high specific surface area ($S = 507 \text{ m}^2 \text{ g}^{-1}$), strong intramolecular hydrogen bonds, and superior specific capacitance of 724 F g^{-1} . [62] Similarly, Khattak et al. synthesized a redox-active covalent organic framework containing pyridine moieties with a specific surface area of $687 \text{ m}^2 \text{ g}^{-1}$ and specific capacitance of 209 F g^{-1} . [63] The abysmal performance of our materials can be attributed to low specific surface area ($195.73 \text{ m}^2 \text{ g}^{-1}$ for MOP and $33.17 \text{ m}^2 \text{ g}^{-1}$), lack of abundant accessible redox active centers, poorly optimized pore structures and inadequate extensive conjugations. [64]

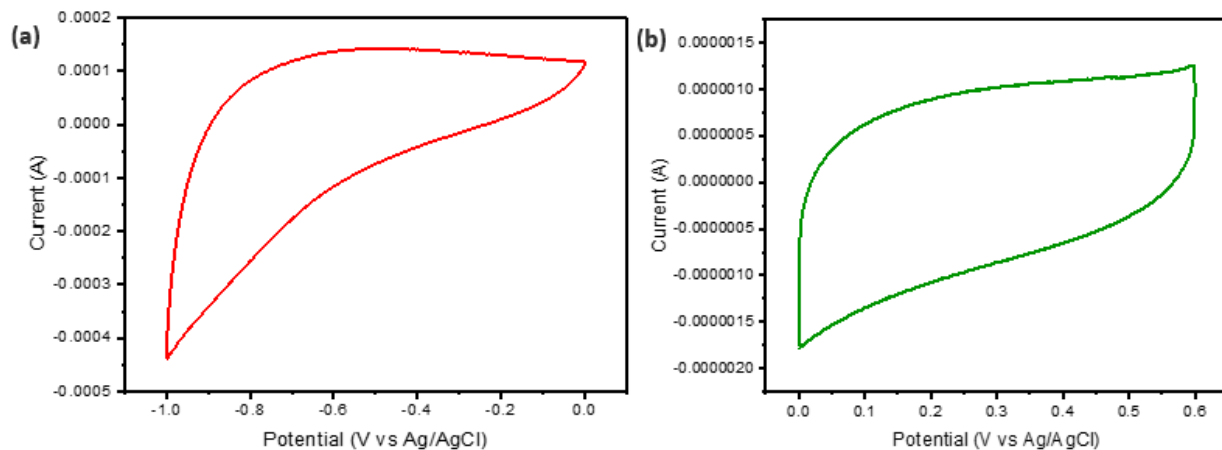


Figure 3-18: Cyclic Voltammetry (CV) curves of (a) MOP; (b) CB[6]-porphyrin framework; at a scan rate of 100mVs^{-1} in 6M KOH

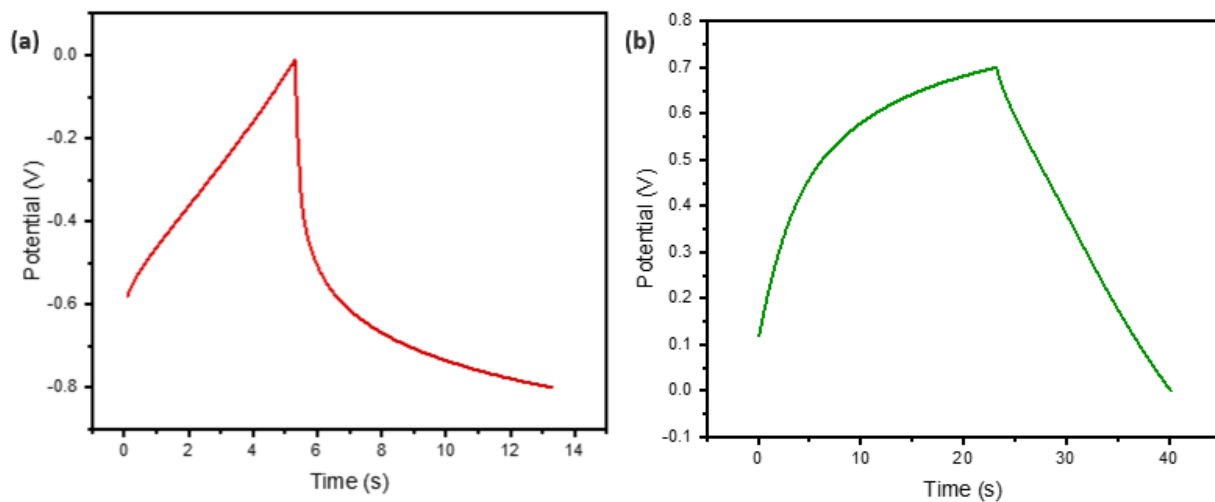


Figure 3-19: Galvanostatic Charge-Discharge (GCD) curves of (a) MOP at current density of 0.1mA^{-1} ; (b) CB[6]-porphyrin framework at a current density of 0.001mA^{-1}

CHAPTER 4

CONCLUSION AND FUTURE WORKS

In conclusion, through the polycondensation reaction between melamine and 2,5-thiophenedicarboxaldehyde, a microporous organic polymer (MOP) was successfully synthesized and then thoroughly characterized. The MOP is a promising candidate for electrocatalytic hydrogen evolution from water splitting due to its heteroatom-rich structure and electron transport capabilities. Here, loading the MOP with Ni increased its HER electrocatalytic performance. The effect of various Ni contents on the HER activity of MOP in 0.5 M KOH was studied, and Ni₂@MOP containing 47% Ni (relative to the MOP) was found to be the best electrocatalyst, producing the lowest onset potential of -66 mV, the highest exchange current density of 0.439 mA cm⁻², and the highest Tafel slope of 212 mV dec⁻¹. Additionally, the Ni₂@MOP electrocatalyst displayed long-term HER catalysis endurance by maintaining a nearly constant current density (10 mA cm⁻²) over the course of 3.5 hours and a high Faradaic efficiency of about 91 %. Here, the created Ni₂@MOP's HER activity was on par with or better than that of a number of non-noble metallic and porous electrocatalysts described in the literature as summarized in Table A.1.

The structural peculiarities of the building blocks of MOP and CB[6]-porphyrin framework, and the preliminary investigation using cyclic voltammetry suggests potential as electrode materials for supercapacitors. However, further investigation using galvanostatic charge-discharge (GCD) revealed an overall poor performance. This may be

attributed to structural inadequacies such as lack easily accessible pores and inadequate redox-active sites. Increasing the surface area and tuning the pore size to appropriately match the size of the electrolyte for easy navigation through the electrode-electrolyte interface will help improve the performance of the materials towards energy storage application. Furthermore, introducing additional easily accessible redox active sites will go a long way towards improving the applicability of the materials towards supercapacitors.

REFERENCES

- [1] N. S. Lewis and D. G. Nocera, "Powering the planet: Chemical Challenges in Solar Energy Utilization," *Proc. Natl. Acad. Sci. U. S. A.*, vol. 103, no. 43, pp. 15729–15735, 2006, doi: 10.1073/pnas.0603395103.
- [2] J. Zhu, L. Hu, P. Zhao, L. Y. S. Lee, and K. Y. Wong, "Recent Advances in Electrocatalytic Hydrogen Evolution Using Nanoparticles," *Chem. Rev.*, vol. 120, no. 2, pp. 851–918, 2020, doi: 10.1021/acs.chemrev.9b00248.
- [3] P. J. Megia, A. J. Vizcaino, J. A. Calles, and A. Carrero, "Hydrogen Production Technologies: From Fossil Fuels toward Renewable Sources. A Mini Review," *Energy and Fuels*, vol. 35, no. 20, pp. 16403–16415, 2021, doi: 10.1021/acs.energyfuels.1c02501.
- [4] A. M. Oliveira, R. R. Beswick, and Y. Yan, "A Green Hydrogen Economy for a Renewable Energy Society," *Curr. Opin. Chem. Eng.*, vol. 33, p. 100701, 2021, doi: 10.1016/j.coche.2021.100701.
- [5] F. Eljack and M.-K. Kazi, "Prospects and Challenges of Green Hydrogen Economy via Multi-Sector Global Symbiosis in Qatar," *Front. Sustain.*, vol. 1, no. January, pp. 1–15, 2021, doi: 10.3389/frsus.2020.612762.
- [6] T. Capurso, M. Stefanizzi, M. Torresi, and S. M. Camporeale, "Perspective of the Role of Hydrogen in the 21st Century Energy Transition," *Energy Convers. Manag.*, vol. 251, no. October 2021, p. 114898, 2022, doi: 10.1016/j.enconman.2021.114898.
- [7] K. Gandhi, H. Apostoleris, and S. Sgouridis, "Catching the Hydrogen Train: Economics-driven Green Hydrogen Adoption Potential in the United Arab Emirates," *Int. J. Hydrogen Energy*, vol. 47, no. 53, pp. 22285–22301, 2022, doi: 10.1016/j.ijhydene.2022.05.055.

- [8] M. Yu, K. Wang, and H. Vredenburg, “Insights into Low-carbon Hydrogen Production Methods: Green, Blue and Aqua hydrogen,” *Int. J. Hydrogen Energy*, vol. 46, no. 41, pp. 21261–21273, 2021, doi: 10.1016/j.ijhydene.2021.04.016.
- [9] C. Bauer *et al.*, “On the Climate Impacts of Blue Hydrogen Production,” *Sustain. Energy Fuels*, vol. 6, no. 1, pp. 66–75, 2022, doi: 10.1039/d1se01508g.
- [10] A. N. Antzaras and A. A. Lemonidou, “Recent Advances on Materials and Processes for Intensified Production of Blue Hydrogen,” *Renew. Sustain. Energy Rev.*, vol. 155, no. April 2021, p. 111917, 2022, doi: 10.1016/j.rser.2021.111917.
- [11] H. An, T. Song, L. Shen, L. Zhang, and B. Feng, “Hydrogen Production from a Victorian Brown Coal with in situ CO₂ capture in a 1 kwth Dual Fluidized-bed Gasification Reactor,” *Ind. Eng. Chem. Res.*, vol. 51, no. 40, pp. 13046–13053, 2012, doi: 10.1021/ie300747m.
- [12] W. W. Clark and J. Rifkin, “A Green Hydrogen Economy,” *Energy Policy*, vol. 34, no. 17, pp. 2630–2639, 2006, doi: 10.1016/j.enpol.2005.06.024.
- [13] S. Atilhan, S. Park, M. M. El-Halwagi, M. Atilhan, M. Moore, and R. B. Nielsen, “Green Hydrogen as an Alternative Fuel for the Shipping Industry,” *Curr. Opin. Chem. Eng.*, vol. 31, p. 100668, 2021, doi: 10.1016/j.coche.2020.100668.
- [14] C. Ri, “ScienceDirect Cost of green hydrogen : Limitations of Production from a Stand-alone Photovoltaic System,” 2022, doi: 10.1016/j.ijhydene.2022.05.090.
- [15] S. Anantharaj, S. R. Ede, K. Sakthikumar, K. Karthick, S. Mishra, and S. Kundu, “Recent Trends and Perspectives in Electrochemical Water Splitting with an Emphasis on Sulfide, Selenide, and Phosphide Catalysts of Fe, Co, and Ni: A Review,” *ACS Catal.*, vol. 6, no. 12, pp. 8069–8097, 2016, doi: 10.1021/acscatal.6b02479.
- [16] C. G. Morales-Guio, L. A. Stern, and X. Hu, “Nanostructured Hydrotreating

- Catalysts for Electrochemical Hydrogen Evolution,” *Chem. Soc. Rev.*, vol. 43, no. 18, pp. 6555–6569, 2014, doi: 10.1039/c3cs60468c.
- [17] C. Wei and Z. J. Xu, “The Comprehensive Understanding of 10 mAcm^{-2} as an Evaluation Parameter for Electrochemical Water Splitting,” *Small Methods*, vol. 2, no. 11, p. 1800168, 2018, doi: 10.1002/smt.201800168.
- [18] F. Bao *et al.*, “Understanding the Hydrogen Evolution Reaction Kinetics of Electrodeposited Nickel-Molybdenum in Acidic, Near-Neutral, and Alkaline Conditions,” *ChemElectroChem*, vol. 8, no. 1, pp. 195–208, 2021, doi: 10.1002/celec.202001436.
- [19] S. Anantharaj *et al.*, “Precision and Correctness in the Evaluation of Electrocatalytic Water Splitting: Revisiting Activity Parameters with a Critical Assessment,” *Energy Environ. Sci.*, vol. 11, no. 4, pp. 744–771, 2018, doi: 10.1039/c7ee03457a.
- [20] D. Lin and A. Lasia, “Electrochemical Impedance Study of the Kinetics of Hydrogen Evolution at a Rough Palladium Electrode in Acidic Solution,” *J. Electroanal. Chem.*, vol. 785, pp. 190–195, 2017, doi: 10.1016/j.jelechem.2016.12.037.
- [21] S. Anantharaj, P. E. Karthik, and S. Noda, “The Significance of Properly Reporting Turnover Frequency in Electrocatalysis Research,” *Angew. Chemie - Int. Ed.*, vol. 60, no. 43, pp. 23051–23067, 2021, doi: 10.1002/anie.202110352.
- [22] P. Du and R. Eisenberg, “Catalysts Made of Earth-abundant Elements (Co, Ni, Fe) for Water Splitting: Recent Progress and Future Challenges,” *Energy Environ. Sci.*, vol. 5, no. 3, pp. 6012–6021, 2012, doi: 10.1039/c2ee03250c.
- [23] S. Popović, M. Smiljanić, P. Jovanović, J. Vavra, R. Buonsanti, and N. Hodnik, “Stability and Degradation Mechanisms of Copper-Based Catalysts for Electrochemical CO₂ Reduction,” *Angew. Chemie - Int. Ed.*, vol. 59, no. 35, pp.

14736–14746, 2020, doi: 10.1002/anie.202000617.

- [24] H. Liu, D. H. Yang, X. Y. Wang, J. Zhang, and B. H. Han, “N-doped Graphitic Carbon Shell-encapsulated FeCo Alloy Derived from Metal–polyphenol Network and Melamine Sponge for Oxygen Reduction, Oxygen Evolution, and Hydrogen Evolution Reactions in Alkaline Media,” *J. Colloid Interface Sci.*, vol. 581, pp. 362–373, 2021, doi: 10.1016/j.jcis.2020.07.055.
- [25] Y. N. Wang *et al.*, “FeCoP₂ Nanoparticles Embedded in N and P Co-doped Hierarchically Porous Carbon for Efficient Electrocatalytic Water Splitting,” *ACS Appl. Mater. Interfaces*, vol. 13, no. 7, pp. 8832–8843, 2021, doi: 10.1021/acsami.0c22336.
- [26] Z. Xiang, D. Cao, L. Huang, J. Shui, M. Wang, and L. Dai, “Nitrogen-doped Holey Graphitic Carbon from 2D Covalent Organic Polymers for Oxygen Reduction,” *Adv. Mater.*, vol. 26, no. 20, pp. 3315–3320, 2014, doi: 10.1002/adma.201306328.
- [27] L. P. Tang *et al.*, “Two-dimensional Porous Coordination Polymers and Nano-Composites for Electrocatalysis and Electrically Conductive Applications,” *J. Mater. Chem. A*, vol. 8, no. 29, pp. 14356–14383, 2020, doi: 10.1039/d0ta03356a.
- [28] C. Y. Lin, L. Zhang, Z. Zhao, and Z. Xia, “Design Principles for Covalent Organic Frameworks as Efficient Electrocatalysts in Clean Energy Conversion and Green Oxidizer Production,” *Adv. Mater.*, vol. 29, no. 17, 2017, doi: 10.1002/adma.201606635.
- [29] S. Maiti, A. R. Chowdhury, and A. K. Das, “Electrochemically Facile Hydrogen Evolution Using Ruthenium Encapsulated Two Dimensional Covalent Organic Framework (2D COF),” *ChemNanoMat*, vol. 6, no. 1, pp. 99–106, 2020, doi: 10.1002/cnma.201900499.
- [30] S. Das, P. Heasman, T. Ben, and S. Qiu, “Porous Organic Materials: Strategic

- Design and Structure-Function Correlation,” *Chem. Rev.*, vol. 117, no. 3, pp. 1515–1563, 2017, doi: 10.1021/acs.chemrev.6b00439.
- [31] B. Ball, C. Chakravarty, and P. Sarkar, “Silicon and Phosphorus Co-doped Bipyridine-linked Covalent Triazine Framework as a Promising Metal-free Catalyst for Hydrogen Evolution Reaction: A Theoretical Investigation,” *J. Phys. Chem. Lett.*, vol. 11, no. 4, pp. 1542–1549, 2020, doi: 10.1021/acs.jpcclett.9b03876.
- [32] B. C. Patra *et al.*, “A Metal-Free Covalent Organic Polymer for Electrocatalytic Hydrogen Evolution,” *ACS Catal.*, vol. 7, no. 9, pp. 6120–6127, 2017, doi: 10.1021/acscatal.7b01067.
- [33] S. Bhunia *et al.*, “Electrochemical Stimuli-Driven Facile Metal-Free Hydrogen Evolution from Pyrene-Porphyrin-Based Crystalline Covalent Organic Framework,” *ACS Appl. Mater. Interfaces*, vol. 9, no. 28, pp. 23843–23851, 2017, doi: 10.1021/acsami.7b06968.
- [34] W. Wang *et al.*, “Tricycloquinazoline-containing 3D Conjugated Microporous Polymers and 2D Covalent Quinazoline Networks: Microstructure and Conductivity,” *Polym. Chem.*, vol. 12, no. 5, pp. 650–659, 2021, doi: 10.1039/d0py01615b.
- [35] K. Chandran Ranjeesh, R. Illathvalappil, V. Chandrakant Wakchaure, Goudappagouda, S. Kurungot, and S. S. Babu, “Metalloporphyrin Two-Dimensional Polymers via Metal-Catalyst-Free C-C Bond Formation for Efficient Catalytic Hydrogen Evolution,” *ACS Appl. Energy Mater.*, vol. 1, no. 11, pp. 6442–6450, 2018, doi: 10.1021/acsaem.8b01381.
- [36] A. Wang, L. Cheng, W. Zhao, X. Shen, and W. Zhu, “Electrochemical Hydrogen and Oxygen Evolution Reactions from a Cobalt-porphyrin-based Covalent Organic Polymer,” *J. Colloid Interface Sci.*, vol. 579, pp. 598–606, 2020, doi: 10.1016/j.jcis.2020.06.109.

- [37] A. Khaligh, Y. Sheidaei, and D. Tuncel, “Covalent Organic Framework Constructed by Clicking Azido Porphyrin with Perpropargyloxy-Cucurbit[6]uril for Electrocatalytic Hydrogen Generation from Water Splitting,” *ACS Appl. Energy Mater.*, vol. 4, no. 4, pp. 3535–3543, 2021, doi: 10.1021/acsaem.0c03265.
- [38] P. Yang and W. Mai, “Flexible Solid-state Electrochemical Supercapacitors,” *Nano Energy*, vol. 8, pp. 274–290, 2014, doi: 10.1016/j.nanoen.2014.05.022.
- [39] X. Liu, C. F. Liu, W. Y. Lai, and W. Huang, “Porous Organic Polymers as Promising Electrode Materials for Energy Storage Devices,” *Adv. Mater. Technol.*, vol. 5, no. 9, pp. 1–20, 2020, doi: 10.1002/admt.202000154.
- [40] L. Li, F. Lu, H. Guo, and W. Yang, “A New Two-dimensional Covalent Organic Framework with Intralayer Hydrogen Bonding as Supercapacitor Electrode Material,” *Microporous Mesoporous Mater.*, vol. 312, no. May 2020, 2021, doi: 10.1016/j.micromeso.2020.110766.
- [41] B. C. Patra, S. Khilari, L. Satyanarayana, D. Pradhan, and A. Bhaumik, “A New Benzimidazole-based Covalent Organic Polymer Having High Energy Storage Capacity,” *Chem. Commun.*, vol. 52, no. 48, pp. 7592–7595, 2016, doi: 10.1039/c6cc02011a.
- [42] P. Bhanja *et al.*, “A New Triazine-Based Covalent Organic Framework for High-Performance Capacitive Energy Storage,” *ChemSusChem*, vol. 10, no. 5, pp. 921–929, 2017, doi: 10.1002/cssc.201601571.
- [43] C. Liu *et al.*, “One-pot Synthesis of Nitrogen-rich Amino- and Triazine-based Hierarchical Porous Organic Polymers with Highly Efficient Iodine Adsorption,” *Polymer (Guildf.)*, vol. 194, no. March, p. 122401, 2020, doi: 10.1016/j.polymer.2020.122401.
- [44] L. Liu, C. Song, and A. Kong, “Nitrogen and Sulfur-enriched Porous Bithiophene-Melamine Covalent Organic Polymers for Effective Capture of CO₂ and Iodine,”

- Mater. Lett.*, vol. 277, p. 128291, 2020, doi: 10.1016/j.matlet.2020.128291.
- [45] M. G. Schwab, B. Fassbender, H. W. Spiess, A. Thomas, X. Feng, and K. Müllen, “Catalyst-free Preparation of Melamine-based Microporous Polymer Networks through Schiff Base Chemistry,” *J. Am. Chem. Soc.*, vol. 131, no. 21, pp. 7216–7217, 2009, doi: 10.1021/ja902116f.
- [46] C. Han *et al.*, “Realizing High Hydrogen Evolution Activity Under Visible Light Using Narrow Band Gap Organic Photocatalysts,” *Chem. Sci.*, vol. 12, no. 5, pp. 1796–1802, 2021, doi: 10.1039/d0sc05866a.
- [47] H. Li, S. Gan, H. Wang, D. Han, and L. Niu, “Intercorrelated Superhybrid of AgBr Supported on Graphitic-C₃N₄-Decorated Nitrogen-Doped Graphene: High Engineering Photocatalytic Activities for Water Purification and CO₂ Reduction,” *Adv. Mater.*, vol. 27, no. 43, pp. 6906–6913, 2015, doi: 10.1002/adma.201502755.
- [48] G. Li, B. Zhang, J. Yan, and Z. Wang, “Tetraphenyladamantane-based Polyaminals for Highly Efficient Captures of CO₂ and Organic Vapors,” *Macromolecules*, vol. 47, no. 19, pp. 6664–6670, 2014, doi: 10.1021/ma501497c.
- [49] J. Mahmood *et al.*, “Two-dimensional Amine and Hydroxy Functionalized Fused Aromatic Covalent Organic Framework,” *Commun. Chem.*, vol. 3, no. 1, pp. 1–6, 2020, doi: 10.1038/s42004-020-0278-1.
- [50] P. J. Waller, F. Gándara, and O. M. Yaghi, “Chemistry of Covalent Organic Frameworks,” *Acc. Chem. Res.*, vol. 48, no. 12, pp. 3053–3063, 2015, doi: 10.1021/acs.accounts.5b00369.
- [51] M. Rong, L. Yang, C. Yang, J. Yu, and H. Liu, “Tetraphenyladamantane-based Microporous Polyaminals for Efficient Adsorption of CO₂, H₂ and Organic Vapors,” *Microporous Mesoporous Mater.*, vol. 323, no. May, p. 111206, 2021, doi: 10.1016/j.micromeso.2021.111206.

- [52] R. Sandín, M. González-Lucas, P. A. Sobarzo, C. A. Terraza, and E. M. Maya, “Microwave-assisted Melamine-based Polyaminals and their Application for Metal Cations Adsorption,” *Eur. Polym. J.*, vol. 155, no. 2021, 2021, doi: 10.1016/j.eurpolymj.2021.110562.
- [53] M. Chhetri, S. Maitra, H. Chakraborty, U. V. Waghmare, and C. N. R. Rao, “Superior Performance of Borocarbonitrides, BxCyNz, as Stable, Low-cost Metal-free Electrocatalysts for the Hydrogen Evolution Reaction,” *Energy Environ. Sci.*, vol. 9, no. 1, pp. 95–101, 2016, doi: 10.1039/c5ee02521d.
- [54] B. Aoudi, A. Khaligh, Y. Sheidaei, and D. Tuncel, “In-situ Electrochemically Reduced Graphene Oxide Integrated with Cross-linked Supramolecular Polymeric Network for Electrocatalytic Hydrogen Evaluation Reaction,” *Polymer (Guildf)*, vol. 231, no. May, pp. 1–12, 2021, doi: 10.1016/j.polymer.2021.124140.
- [55] S. S. Shinde, A. Sami, D. H. Kim, and J. H. Lee, “Nanostructured SnS-N-doped Graphene as an Advanced Electrocatalyst for the Hydrogen Evolution Reaction,” *Chem. Commun.*, vol. 51, no. 86, pp. 15716–15719, 2015, doi: 10.1039/c5cc05644f.
- [56] J. Guo, F. Li, Y. Sun, X. Zhang, and L. Tang, “Oxygen-incorporated MoS₂ Ultrathin Nanosheets Grown on Graphene for Efficient Electrochemical Hydrogen Evolution,” *J. Power Sources*, vol. 291, pp. 195–200, 2015, doi: 10.1016/j.jpowsour.2015.05.034.
- [57] L. Chen *et al.*, “Metal-organic Framework-based Composite Ni@MOF as Heterogenous Catalyst for Ethylene Trimerization,” *Appl. Catal. A Gen.*, vol. 594, no. October 2019, p. 117457, 2020, doi: 10.1016/j.apcata.2020.117457.
- [58] K. Rui *et al.*, “Hybrid 2D Dual-Metal–Organic Frameworks for Enhanced Water Oxidation Catalysis,” *Adv. Funct. Mater.*, vol. 28, no. 26, pp. 1–9, 2018, doi: 10.1002/adfm.201801554.

- [59] R. Karthikeyan, D. Thangaraju, N. Prakash, and Y. Hayakawa, "Single-step Synthesis and Catalytic Activity of Structure-controlled Nickel Sulfide Nanoparticles," *CrystEngComm*, vol. 17, no. 29, pp. 5431–5439, 2015, doi: 10.1039/c5ce00742a.
- [60] H. Bin Yang *et al.*, "Atomically Dispersed Ni(i) as the Active Site for Electrochemical CO₂ Reduction," *Nat. Energy*, vol. 3, no. 2, pp. 140–147, 2018, doi: 10.1038/s41560-017-0078-8.
- [61] K. Rajalakshmi *et al.*, "Fabrication of Thiophene Decorated Side Chain Entanglement Free COFs for Highly Regenerable Mercury Extraction," *Chem. Eng. J.*, vol. 430, no. P4, p. 133149, 2022, doi: 10.1016/j.cej.2021.133149.
- [62] T. Li *et al.*, "A 2D Covalent Organic Framework Involving Strong Intramolecular Hydrogen Bonds for Advanced Supercapacitors," *Polym. Chem.*, vol. 11, no. 1, pp. 47–52, 2019, doi: 10.1039/c9py01623f.
- [63] A. M. Khattak *et al.*, "A redox-active 2D Covalent Organic Framework with Pyridine Moieties Capable of Faradaic Energy Storage," *J. Mater. Chem. A*, vol. 4, no. 42, pp. 16312–16317, 2016, doi: 10.1039/c6ta05784e.
- [64] X. Liu *et al.*, "Porous Organic Polymers for High-performance Supercapacitors," *Chem. Soc. Rev.*, pp. 3181–3225, 2022, doi: 10.1039/d2cs00065b.
- [65] W. F. Chen *et al.*, "Hydrogen-evolution Catalysts Based on Non-noble Metal Nickel-molybdenum Nitride Nanosheets," *Angew. Chemie - Int. Ed.*, vol. 51, no. 25, pp. 6131–6135, 2012, doi: 10.1002/anie.201200699.
- [66] A. J. Clough, J. W. Yoo, M. H. Mecklenburg, and S. C. Marinescu, "Two-dimensional Metal-organic Surfaces for Efficient Hydrogen Evolution from Water," *J. Am. Chem. Soc.*, vol. 137, no. 1, pp. 118–121, 2015, doi: 10.1021/ja5116937.

- [67] C. A. Downes and S. C. Marinescu, "Efficient Electrochemical and Photoelectrochemical H₂ Production from Water by a Cobalt Dithiolene One-Dimensional Metal-Organic Surface," *J. Am. Chem. Soc.*, vol. 137, no. 43, pp. 13740–13743, 2015, doi: 10.1021/jacs.5b07020.
- [68] D. Zhou, X. Tan, H. Wu, L. Tian, and M. Li, "Synthesis of C–C Bonded Two-Dimensional Conjugated Covalent Organic Framework Films by Suzuki Polymerization on a Liquid–Liquid Interface," *Angew. Chemie - Int. Ed.*, vol. 58, no. 5, pp. 1376–1381, 2019, doi: 10.1002/anie.201811399.
- [69] D. A. Dalla Corte, C. Torres, P. D. S. Correa, E. S. Rieder, and C. D. F. Malfatti, "The Hydrogen Evolution Reaction on Nickel-polyaniline Composite Electrodes," *Int. J. Hydrogen Energy*, vol. 37, no. 4, pp. 3025–3032, 2012, doi: 10.1016/j.ijhydene.2011.11.037.
- [70] T. Wang, X. Li, Y. Jiang, Y. Zhou, L. Jia, and C. Wang, "Reduced Graphene Oxide-polyimide/carbon Nanotube Film Decorated with NiSe Nanoparticles for Electrocatalytic Hydrogen Evolution Reactions," *Electrochim. Acta*, vol. 243, pp. 291–298, 2017, doi: 10.1016/j.electacta.2017.05.084.

APPENDIX

Table A.1. A comparison of electrochemical parameters of different non-noble metal electrocatalysts.

Composite	Electrolyte	Onset (mV)	$\eta@10\text{mAcm}^{-2}$ (mV)	Ref.
NiMoN _x /C ^a	0.1 M HClO ₄	-78 vs RHE	---	[65]
THT-Co ^b	1.3 M H ₂ SO ₄	320 vs RHE	530 vs RHE	[66]
BTT-Co ^c	1.3 M H ₂ SO ₄	---	-560 vs RHE	[67]
12%Ni@COF-TPP-CB[6] ^d	0.1 M KOH	-250 vs RHE	-914 vs RHE	[37]
Ni ₂ @PCN ^e	0.1 M KOH	-253 vs RHE	-894 vs RHE	[54]
GO ₁ /Ni ₂ @PCN ^f	0.1 M KOH	-145 vs RHE	-879 vs RHE	[54]
COF film ^g	0.5 M H ₂ SO ₄	---	-541 vs RHE	[68]
Ni-PAni 175 ^h	0.5 M H ₂ SO ₄	-82mV vs RHE	---	[69]
MoSe ₂ -rGO-PI ⁱ	0.5 M H ₂ SO ₄	540 vs RHE current density of 5 mA cm ⁻²	---	[70]

Ni₂@MOP	0.5 M KOH	-66 vs RHE	-597 vs RHE	This work
---------------------------	-----------	------------	-------------	----------------------

^a carbon-supported nickel–molybdenum nitride, ^b Cobalt 2,3,6,7,10,11-triphenylene-hexathiol, ^c Cobalt benzene-1,2,4,5-tetrathiolate, ^d 12% Ni loaded cucurbituril-azido-functionalized tetraphenylporphyrin covalent organic framework, ^e Nickel Functionalized polymeric network, ^f Graphene-oxide-Nickel Functionalized polymeric network, ^g Covalent Organic Framework Films, ^h nickel-polyaniline composite (175l-1 of Polyaniline), ⁱ MoSe₂-Reduced Graphene Oxide/Polyimide Composite Film